Numerical relativity simulations of neutron star merger remnants using conservative mesh refinement

Tim Dietrich[1], Sebastiano Bernuzzi[2,3], Maximiliano Ujevic[4], and Bernd Brügmann[1]

[1] *Theoretical Physics Institute, University of Jena, 07743 Jena, Germany*
[2] *Theoretical Astrophysics, California Institute of Technology,*
1200 E California Blvd,Pasadena, California 91125, USA
[3] *DiFeST, University of Parma, and INFN Parma, I-43124 Parma, Italy and*
[4] *Centro de Ciências Naturais e Humanas, Universidade Federal do ABC, 09210-170, Santo André, São Paulo, Brazil*

We study equal and unequal-mass neutron star mergers by means of new numerical relativity simulations in which the general relativistic hydrodynamics solver employs an algorithm that guarantees mass conservation across the refinement levels of the computational mesh. We consider eight binary configurations with total mass $M = 2.7 \, M_\odot$, mass-ratios $q = 1$ and $q = 1.16$, and four different equations of state (EOSs), and one configuration with a stiff EOS, $M = 2.5 M_\odot$ and $q = 1.5$, which is one of the largest mass ratio simulated in numerical relativity to date. We focus on the post-merger dynamics and study the merger remnant, dynamical ejecta and the postmerger gravitational wave spectrum. Although most of the merger remnant are a hypermassive neutron star collapsing to a black hole+disk system on dynamical timescales, stiff EOSs can eventually produce a stable massive neutron star. During the merger process and on very short timescales, about $\sim 10^{-3} - 10^{-2} \, M_\odot$ of material become unbound with kinetic energies $\sim 10^{50}$erg. Ejecta are mostly emitted around the orbital plane; and favored by large mass ratios and softer EOS. The postmerger wave spectrum is mainly characterized by the non-axisymmetric oscillations of the remnant neutron star. The stiff EOS configuration consisting of a $1.5 M_\odot$ and a $1.0 M_\odot$ neutron star, simulated here for the first time, shows a rather peculiar dynamics. During merger the companion star is very deformed; about $\sim 0.03 M_\odot$ of rest-mass becomes unbound from the tidal tail due to the torque generated by the two-core inner structure. The merger remnant is a stable neutron star surrounded by a massive accretion disk of rest-mass $\sim 0.3 M_\odot$. This and similar configurations might be particularly interesting for electromagnetic counterparts. Comparing results obtained with and without the conservative mesh refinement algorithm, we find that post-merger simulations can be affected by systematic errors if mass conservation is not enforced in the mesh refinement strategy. However, mass conservation also depends on grid details and on the artificial atmosphere setup; the latter are particularly significant in the computation of the dynamical ejecta.

I. INTRODUCTION

Binary neutron star (BNS) mergers are extreme events associated to a variety of observable phenomena in the gravitational and electromagnetic spectra, e.g. [1–3]. BNS coalescence is primarily driven by the emission of gravitational waves (GWs). Indirect evidence for GWs has been indeed inferred by radio observation of double pulsars [4–8], but a direct detection of GWs is still pending. The GW signal emitted during the last minutes of the coalescence and merger is in the band of ground-based laser interferometer network made of LIGO [9] and Virgo [10]. Within the next years, this network will start to operate at sensitivities where $\sim 0.4 - 400$ detections per year are expected [11, 12]. Several electromagnetic counterparts are expected both during and following BNS mergers; joint observations of the gravitational and electromagnetic emissions will maximize the scientific returns [13]. Neutron star mergers are usually associated to short-gamma ray burst (and afterglows) [1, 14]. Although the precise injection mechanism has not been clearly identified, BNSs remain the most plausible triggers of these powerful emissions. Dynamical ejecta from BNS are currently the most plausible site of origin of heavy nuclei ($A \gtrsim 140$) rapid neutron-capture process [15–17]. The radioactive decay of some of these newly produced heavy elements is likely to lead to strong electromagnetic transients called kilonova (or macronova) events [18–21]. Finally, a large amount of energy is released in neutrinos, produced by the merger remnant either via shocks [22, 23] and neutron-rich outflows [24], or, at lower energies, in the hot dense regions of the hypermassive neutron star (HMNS) [25, 26]. However, the steep energy dependence of neutrinos of the interaction cross sections and their moderate energies (~ 20 MeV) make them hard to detect.

Modeling BNS mergers requires relativistic hydrodynamics simulations in dynamical spacetimes, i.e. the solution of the full set of Einstein's field equations. General relativistic BNS simulations are typically performed in the framework of 3+1 numerical relativity using Cartesian-grids, finite volume methods, and explicit time evolutions, see [27] for a review. A crucial ingredient in such numerical setups is the use of adaptive mesh refinement (AMR), in particular the methods of [28], which were implemented for various applications in numerical relativity [29–33]. Nested Cartesian boxes with 2:1 grid spacing refinement and Berger-Oliger time stepping [28] proved to be a robust and stable solution

for the computation of black hole [33–36] and neutron star mergers [37–40] as well as rotational collapse of neutron stars [41–43] or massive stars [44, 45].

One of the main problems in the simulation of hydrodynamical flows with finite volume methods and AMR techniques is to preserve global conservation of mass and other quantities, especially in the presence of shocks, contact discontinuities and large gradients. In a seminal paper, Berger and Colella have proposed a refluxing scheme which guarantees conservation across refinement level [46]. Essentially, the refluxing scheme enforces the fluxes in and out across a coarse/fine cell boundary to be the same to round-off level. Algorithmically it consists in a correction step applied to the solution at certain grid points after each time step.

The importance of a conservative mesh refinement is illustrated in Fig. 1, for the simplest case of the 1D advection equation, $(\partial_t + \partial_x)u(t,x) = 0$ with $x \in [-4,4]$ and discontinuous initial data, $u(0,x) = 1$ for $x \in [-2,-0.2]$, $u(0,x) = 0$ otherwise. We employ a grid composed of 3 fixed levels $l = 0,1,2$ with $n = 800$ grid points, centered around $x = 0$. The coarse level has grid spacing $h_0 = 0.01$ and the others are successively refined by factors two, $h_{l+1}/h_l = 1/2$. Time evolution is performed with a 4th order Runge-Kutta and the Berger-Oliger method; fluxes are computed with a linear reconstruction using the Van Leer MC2 limiter. Figure 1 shows the evolution of the mass of the system on each refinement level, $M^{(l)} = \sum_{i=1}^{n} u_i^{(l)} h_l$, which without mesh refinement (unigrid) is conserved to round off precision. Using mesh refinement, one observes that every time the mass flows in/out a refinement level (see e.g. $t \simeq 1, 1.2, 2.2, ...$, top panel), a mass violation takes place (bottom panel). Notably, the mass either decreases or increases in a way that depends on the scheme's truncation error and that in general is not predictable. Also, after the wave has left all inner refinement levels an error in the mass on $l = 0$ is still present. Instead, using the Berger and Colella correction step, mass conservation is verified at the round-off error, exactly as in the unigrid case.

Conservative AMR schemes have been introduced in numerical relativity only very recently [42, 47]. They have been used to simulate eccentric mergers of both black holes - neutron star and double neutron star systems, including the merger remnant, post-merger disks and ejecta [48, 49]. Also, they have been employed in massive star and core-collapse supernovae evolutions in general relativity [50–52]. Recent studies of rotating neutron star collapse to black hole greatly benefit of the use of conservative AMR, and allowed an accurate calculation of the gravitational wave signal [42, 43] and a local comparison of the end state with black hole spacetimes [53].

In binary simulations one expects that conservative AMR can significantly improve numerical relativity simulations, especially simulations of the merger remnant. A direct comparison of the performance of a conservative mesh refinement algorithm in coalescing BNS systems is presently missing. In the context of spinning equal-mass quasi circular mergers, we have pointed out that the simulation of the hypermassive neutron star is sensitive to the mesh boxes size and their extension [54]. The latter factors influence mass conservation (for a fixed resolution), and a conservative scheme is desirable. Another potentially important application of conservative AMR is the simulations of low-density material in postmerger accretion disks and dynamical ejecta. Ejecta have densities several orders of magnitude smaller than the typical neutron star maximum densities; thus, their calculation employing grid-based codes is very challenging. Dynamical ejecta in full general relativistic BNS merger simulations have been previously studied only in [55, 56] in more detail. Those works do not employ a conservative AMR strategy, thus the accuracy of the result can be, in principle, seriously compromised.

The purpose of this paper is threefold.

First, we present our implementation of a conservative AMR algorithm and present a set of single star spacetime evolutions in which we assess the performances of the algorithm. We focus on the evolution of different single star spacetimes since such tests (i) received little attention in the literature; (ii) are computationally relatively cheap; (iii) are highly nontrivial and preparatory cases for the application of the code to BNs evolutions.

Second, we apply our upgraded code to the study of equal-mass (mass ratio $q = 1$) and unequal-mass ($q = 1.16$) BNS system described by various equations of state (EOS). We directly compare results obtained with and without the conservative AMR. We focus on the postmerger dynamics and investigate the physical properties of the remnant. In particular we study as a function of the EOS and the mass ratio the following properties: (i) the merger outcome; (ii) mass and kinetic energy of the dynamical ejecta; (iii) GW spectra.

Third, we consider for the first time the evolution of a BNS system with a stiff EOS and mass ratio $q = 1.5$ (total mass $M = 2.5 M_\odot$). This binary has the largest mass ratio simulated so far (see also [57]). The particular combination of EOS, q, and total mass properties lead to a peculiar merger remnant composed of a *stable* massive neutron star surrounded by an extended, massive accretion disk. Also, the binary configuration favors mass ejection during merger. These kind of binary configurations are possible and might be particular relevant for electromagnetic counterparts. However, they have received little attention in numerical relativity, although some recent observations are in favor for a stiff EOS [58, 59].

The article is structured as follows. After a brief review of the equations (Sec. II), we present our numerical strategy in Sec. III focusing on the novel implementation of the conservative mesh refinement. Section IV describes the main quantities employed for the analysis of our BNS simulations. In Sec. V we describe a variety of single star tests in which the performance of the conservative AMR is investigated for different combinations of the relevant parameters of

the simulations (restriction and prolongation operators and artificial atmosphere parameters.) Section VI summarizes the BNS configurations and the grid setup used for evolutions. In Sec. VII we apply the new algorithm and evolve 16 BNS systems with mass ratios $q = 1$ and $q = 1.16$ and different EOS. In Sec. VIII we consider a BNS with $q = 1.5$, total mass $M = 2.5M_\odot$, and the stiff equation of state MS1b. Finally, the conclusions are presented in Sec. IX. Throughout this article, geometrical units $c = G = M_\odot = 1$ are employed unless otherwise stated. At some places units of $M_\odot$ are given explicitly for clarity.

II. SUMMARY OF THE EQUATIONS

Let us summarize briefly the most important equations employed in this work. We work with the 3+1 formalism (e.g. [60]) and indicate with γ_{ij} the 3-metric, and with α and β^i the lapse and shift vector.

General-relativistic hydrodynamics (GRHD) equations are solved in conservative form,

$$\partial_t \vec{q} = -\partial_i \vec{f^i} + \vec{s}\,, \tag{1}$$

with $\vec{q} = \sqrt{\gamma}(D, S_i, \tau)$ being the vector of the Eulerian conservative variables defined in terms of the primitive variables as,

$$D = W\rho,\ S_i = W^2 \rho h v_i,\ \tau = (W^2 \rho h - p) - D. \tag{2}$$

The primitive variables are the rest-mass density ρ, the pressure p, the specific internal energy ϵ, and the 3-velocity v^i. Additionally, we define the Lorentz factor $W = 1/\sqrt{1 - v_i v^i}$, the enthalpy $h = 1 + \epsilon + p/\rho$, and the determinant of the 3-metric γ. On the right-hand-side of Eq. (1) one has the divergence of the fluxes and source terms depending on the metric, metrics first derivatives and fluid variables. We stress that only the first equation of (1) is a "strict" conservation law,

$$\partial_t q^{(D)} + \partial_i f^{(D)\,i} = 0\,, \tag{3}$$

in the sense that the source term is zero and a conserved quantity can be associated: the rest-mass M_b. We refer to [61, 62] for an extensive discussion of these equations.

The PDE system in (1) is closed by an equation of state (EOS) in the form $p = P(\rho, \epsilon)$. A simple EOS is the Γ-law $P(\rho, \epsilon) = (\Gamma - 1)\rho\epsilon$, or its barotropic version $P(\rho) = K\rho^\Gamma$ (polytropic EOS). Several barotropic – zero-temperature EOS developed to describe neutron star matter can be fit with piecewise polytropic models, and efficiently used in simulations. In our work we employ four segment fitting models following the construction of [63]. Each segment is given by a certain rest-mass density interval $\rho_i < \rho < \rho_{i+1}$; the pressure is then calculated as $P(\rho) = K_i \rho^{\Gamma_i}$ where the polytropic constants K_i are determined by demanding continuity of $P(\rho)$ at the interfaces, $K_i \rho^{\Gamma_i} = K_{i+1} \rho^{\Gamma_{i+1}}$. The parameters of our EOS are reported in Tab. A; notice that we specify ρ_0 in our units. Thermal effects are simulated with an additive thermal contribution in the pressure in a Γ-law form, $P_{th} = (\Gamma_{th} - 1)\rho\epsilon$, with $\Gamma_{th} = 1.75$, see [38, 40, 64].

The Einstein equations are written in 3+1 form, either as the BSSN [65–67] or the Z4c [68, 69] system. In the gauge sector, we use the 1+log-slicing condition [70] for the lapse and the Gamma driver shift [71, 72]. The fundamental role of this gauge in the numerical simulation of the gravitational collapse and singularity formation/evolution was investigated in different physical scenarios [43, 73–75].

III. NUMERICAL METHOD

In this work we use the numerical relativity methods implemented in the BAM code [33, 34, 40, 76]. Our new implementation of the conservative mesh refinement for hydrodynamics fields is based on the Berger-Colella method [46] and follows [47]; we describe it in detail in this section.

A. Computational Grid

The computational grid is made of a hierarchy of cell-centered nested Cartesian grids. The hierarchy consists of L levels of refinement labeled by $l = 0, ..., L - 1$. A refinement level l has one or more Cartesian grids with constant grid spacing h_l and n points per direction. The grid spacing in each refinement level is refined according to $h_l = h_0/2^l$. The grids are properly nested in such a way that the coordinate extent of any grid at level l, $l > 0$, is completely covered by

the grids at level $l - 1$. Some of the mesh refinement levels $l > l^{\mathrm{mv}}$ can be dynamically moved and adapted during the time evolution according to the technique of "moving boxes", e.g. [33, 39, 77]. BAM's grid can be further extended in the wave zone using a multipatch "cubed-sphere" as described in [69, 78–80]. Every refinement level has buffer zones populated by interpolation; interpolation from the parent (coarse) to the child (fine) level is the *prolongation* (P) operation, the one from the fine to the coarse level is the *restriction* (R) operation. For metric variables these operations are performed with sixth order Lagrangian operators. Spatial interpolation of matter variables is discussed below.

The grid variables are evolved in time with the method of lines, using an explicit fourth order Runge-Kutta and employing the Berger-Oliger (BO) algorithm [28]. For efficiency, we typically use only six buffer zones and perform a linear interpolation in time to update the buffer zones during the Runge-Kutta step, see [33] for more details. A Courant-Friedrich-Lewy factor of 0.25 is employed in all runs, if not stated differently. Standard finite differencing 4th order stencils are employed for the spatial derivatives of the metric. GRHD is solved by means of a high-resolution-shock-capturing method [40] based on primitive reconstruction and the Local-Lax-Friedrich's (LLF) central scheme for the numerical fluxes. Primitive reconstruction is performed with the 5th order WENO scheme of [81] as in [82].

B. Conservative mesh refinement

Let us review the main idea of the new conservative AMR algorithm implemented in the BAM code. Without loss of generality we restrict the presentation to the first equation of (1), and to the flux in the x-direction only. Although the algorithm is applied to all the fluid variables, Eq. (3), the D-equation, is the only one which is a strict conservation law. Directions different from the x direction are treated in a similar way.

The discrete model equation reads,

$$D_{i,j,k}^{n+1} = D_{i,j,k}^{n} - \frac{\Delta t}{\Delta x} \left(F_{i+1/2,j,k}^{x} - F_{i-1/2,j,k}^{x} \right) \tag{4}$$

where $F_{i+1/2,j,k}^{x}$ denotes the x-component of the numerical flux across the cell face $(i + 1/2, j, k)$ (boundary of cell (i, j, k) and $(i + 1, j, k)$), $\Delta x = h$, n denotes the time level, and Δt the time step. Consider the model equation on two sequential levels of refinement with $h_{l+1}/h_l = 1/2$, and on cells at the boundary of refinement $l + 1$. Mass violation happens during a BO step, because: (i) the buffer zones of level $l + 1$ are set by prolongation (P) from level l; (ii) the prolongation carries a certain truncation error, so the fluxes on $l + 1$ differ from those on l; (iii) after restriction (R) from level $l + 1$, the solution on level l is not consistent with the fluxes on l. The process is illustrated in Fig. 2. After the time step Δt, the changes $\delta D_{(i,j,k)}^{(l)}$ of the variable $D^{(l)}$ on level l due to the flux going through the cell face $(i_l + 1/2, j_l, k_l)$ is given by

$$\delta D_{(i,j,k)}^{(l)}(t + \Delta t) = -\frac{\Delta t}{\Delta x} F_{i_l+1/2,j_l,k_l}^{(x)}(t) . \tag{5}$$

After level l, level $l + 1$ advances by two $\Delta t/2$ time steps and one has

$$\delta D_{(i,j,k)}^{(l+1)}(t + \Delta t) = -\frac{\Delta t/2}{\Delta x/2} F_{i_{l+1}+1/2,j_{l+1},k_{l+1}}^{(x)}(t) \tag{6}$$
$$- \frac{\Delta t/2}{\Delta x/2} F_{i_{l+1}+1/2,j_{l+1},k_{l+1}}^{(x)}(t + \Delta t/2) .$$

In general, these two changes are different at truncation error level. Similarly the mass flows across the face are different, $\delta M^{(l+1)} \neq \delta M^{(l)}$, and, after restriction, the mass conservation is violated in a way $\propto \delta M^{(l)} - \delta M^{(l+1)}$.

The original Berger-Colella algorithm corrects the solution at level l after the refinement level $l + 1$ has completed its time step and both levels are time-aligned [46]. The *correction* (C) operation is $D^{(l)} \mapsto D^{(l)} + \Delta t/\Delta x \, \delta F^{(l)}$, where $\delta F^{(l)}$ is a flux correction stored on the cell face. First, $\delta F^{(l)}$ is initialized with $-F_{i_l+1/2,j_l,k_l}^{(x)}$ before advancing in time level $l + 1$. Then, during each time step of level $l + 1$, it receives and sums up the contributions $F_{i_{l+1}+1/2,j_{l+1},k_{l+1}}^{(x)}$ (two contributions in our example). The C step guarantees consistency of the fluxes. East et al. [47] proposed to store the mass correction $\delta M^{(l)}$ rather than $\delta F^{(l)}$, and perform the correction as $D^{(l)} \mapsto D^{(l)} + \delta M^{(l)}/V^{(l)}$ where $V^{(l)}$ is the cell volume [47]. This method is simpler and has the advantage of using grid variables defined on cell centers instead of faces. We follow this approach.

Our implementation is as follows:

1. We introduce a mask to label the cells involved in the C step. These are the innermost buffer points of level $l+1$ (red in Fig. 2) and the corresponding parent cells (blue in Fig. 2). The mask also stores the information about the box face, i.e. one of the possibilities $(\pm x, \pm y, \pm z)$. The mask has to be recomputed after each regridding step.

2. After each evolution step we store the mass change of the parent cells

$$\delta M^{(l)} = \pm V^{(l)} \delta D^{(l)} , \tag{7}$$

and, similarly, after each sub-step, $\delta M^{(l+1)} = +V^{(l)} \delta D^{(l)}$ for level $l+1$. Notice that the particular sign depends on the entry in the mask, e.g. $+x$-surfaces refer to a positive sign in (7).

3. When the parent and the child level are aligned in time, we sum up the contributions and correct the cell values with,

$$D^{(l)} \mapsto D^{(l)} + \frac{\delta M^{(l)}}{V_l} - \sum \frac{\delta M^{(l+1)}}{V_{l+1}} . \tag{8}$$

We observe that the effectiveness of the algorithm depends crucially on the specific RP operators. For hydrodynamics fields the R step is conservative if the operation is performed using local averages, which are second order accurate, $\mathcal{O}(h^2)$. Similarly, a safe choice for the P step is linear interpolation using limiters in order to control oscillations. However, for neutron star spacetime simulations high-order operators may be important for accuracy and faster convergence. As indicated in Tab. II, we have implemented several RP operators, including ENO 2nd order [83], Lagrangian and WENO 4th order [40]. In the next sections we will present results for various combinations of RPC operators using the abbreviations defined in Tab. II.

C. Atmosphere treatment

For the simulation of neutron star spacetimes, the vacuum region outside the stars requires special treatment. As described in [40], we use a low-density static and barotropic atmosphere at a density level

$$\rho_{atm} = f_{atm} \ \text{max}[\rho(t=0)]. \tag{9}$$

During the recovery of the primitive variables from the conservative variables, a point is set to atmosphere if the density is below the threshold

$$\rho_{thr} = f_{thr} \ \rho_{atm}. \tag{10}$$

The atmosphere treatment violates mass conservation and can potentially affect, or invalidate, the improvements related to the conservative AMR. In the following we will investigate this aspect in some detail experimenting with parameters $f_{atm} \in [10^{-13}, 10^{-9}]$ and $f_{thr} = (10^1, 10^2, 10^3, 10^4)$ (see in particular Sec. V 3).

IV. SIMULATION ANALYSIS

In this section we describe the quantities employed for the analysis of our simulations. Notably, we introduce some diagnostic which are helpful to investigate the energetics/geometry of the ejected material.

The performances of the conservative AMR scheme are mainly tested using the baryonic, or rest-mass, mass integral,

$$M_b = \int \mathrm{d}^3x \ q^{(D)} = \int \mathrm{d}^3x \ \sqrt{\gamma} \ D , \tag{11}$$

which should remain constant during the evolution, compare Eq. (3). The rest-mass, and the other integrals discussed in this work, are calculated on each refinement level. We usually report results for a given level, which is the appropriate one for the particular quantity; e.g. the baryonic mass is reported on the $l = 1, 2$ level.

The merger remnant of several BNS configurations considered here is a hypermassive neutron star (HMNS) which collapses to black hole on a dynamical timescale. The lifetime τ_{HMNS} is typically calculated from the moment of merger (see below) to the time an apparent horizon forms. The black hole is then characterized by its horizon mass M_{BH} and spin j_{BH} computed from the apparent horizon with average radius r_{AH}.

The rest-mass of the accretion disk that forms after collapse is computed as,

$$M_{\mathrm{disk}} = \int_{r>r_{\mathrm{AH}}} \mathrm{d}^3x \ q^{(D)} \ , \tag{12}$$

where the domain of integration excludes the spherical region inside the apparent horizon.

The ejected material is defined by the two conditions,

$$u_t < -1 \ \ \mathrm{and} \ \ \bar{v}_r = v^i x_i > 0 \ , \tag{13}$$

where $u_t = -W(\alpha - \beta_i v^i)$ is the first lower component of the fluid 4-velocity, and $x^i = (x, y, z)$. The first condition in (13) assumes fluid elements follow geodesics and requires that the orbit is unbound. This is a simple criterion we use for continuity with previous work, e.g. [49, 55], and should at least capture the correct order of magnitude. The condition $\bar{v}_r > 0$ requires that the material has an outward pointing radial velocity; it has been used in [49] but not in [55]. The total ejecta mass is computed as,

$$M_{\mathrm{ejecta}} = \int_{\mathcal{U}} \mathrm{d}^3x \ q^{(D)} \ , \tag{14}$$

where the integral is computed on the region,

$$\mathcal{U} = \{x^i = (x, y, z) \ : \ u_t < -1 \ \ \mathrm{and} \ \ \bar{v}_r > 0\} \ , \tag{15}$$

on which material is unbound according to (13).

In order to investigate the energetics and geometry of the ejecta we consider different sets of integrals in the (x, y)-plane, in the (x, z)-plane, and the full 3D-domain. The kinetic energy of the ejecta can be approximated as the difference between the total energy E_{ejecta} (excluding gravitational potential energy), and the rest-mass and the total internal energy U_{ejecta} [55],

$$T_{\mathrm{ejecta}} = E_{\mathrm{ejecta}} - (M_{\mathrm{ejecta}} + U_{\mathrm{ejecta}})$$
$$= \int_{\mathcal{U}} \mathrm{d}^3x \ D(e - 1 - \epsilon) \ , \tag{16}$$

where $e = \alpha u^t h - p/(\rho \alpha u^t)$. Additionally, we compute the D-weighted integral of $v^2 = v_i v^i$,

$$\langle v \rangle_\rho = \left(\frac{\int_{\mathcal{U}} \mathrm{d}x \mathrm{d}y \ D v^2}{\int_{\mathcal{U}} \mathrm{d}x \mathrm{d}y \ D} \right)^{1/2} \ , \tag{17}$$

$$\langle v \rangle_z = \left(\frac{\int_{\mathcal{U}} \mathrm{d}x \mathrm{d}z \ D v^2}{\int_{\mathcal{U}} \mathrm{d}x \mathrm{d}z \ D} \right)^{1/2} \ , \tag{18}$$

and the quantities,

$$\langle \rho \rangle = \left(\frac{\int_{\mathcal{U}} \mathrm{d}x \mathrm{d}y \ D \ (x^2 + y^2)}{\int_{\mathcal{U}} \mathrm{d}x \mathrm{d}y \ D} \right)^{1/2} \ , \tag{19}$$

$$\langle z \rangle = \left(\frac{\int_{\mathcal{U}} \mathrm{d}x \mathrm{d}z \ D \ z^2}{\int_{\mathcal{U}} \mathrm{d}x \mathrm{d}z \ D} \right)^{1/2} \ . \tag{20}$$

$\langle \rho \rangle$ and $\langle z \rangle$ roughly estimate the geometric distribution of the ejecta. Similar integrals have been proposed in [55], but in that case they were employed in three dimensions. We will use the approximation of the kinetic energy T_{ejecta} in Sec. VII A and discuss the weighted velocities $\langle v \rangle_{\rho,z}$ and the $\langle \rho \rangle, \langle z \rangle$ for the case-study in Sec. VIII.

We compute the entropy "indicator",

$$\hat{S} = \frac{p}{K_i \rho^{\Gamma_i}}, \tag{21}$$

where Γ_i and K_i are locally determined by the value of ρ, see Tab. A. In cases where the additional thermal contribution to the pressure P_{th} is small $\hat{S} \sim 1$, while in presence of shock heating $\hat{S} \gg 1$.

Finally, gravitational waveforms are calculated via the curvature invariant Ψ_4 and performing multipole decomposition on extraction spheres [33]. We work with the metric multipoles $rh_{\ell m}$, which are reconstructed from the curvature multipoles using the frequency domain integration of [85], using the initial circular gravitational wave frequency as a cutting frequency, see Tab. IV. All the waveforms are plotted against the retarded time,

$$u = t - r_* = t - r_{\mathrm{extr}} - 2M \ln \left(r_{\mathrm{extr}}/2M - 1 \right), \tag{22}$$

where the extraction radius is $r_{\mathrm{extr}} \sim 750 \, M_\odot$.

V. SINGLE NEUTRON STAR TESTS

Our conservative AMR implementation has been tested and validated in full-general relativistic simulations of single star spacetimes. In this section, we present five different tests, namely

TOV$_{static}$ a static (nonrotating) neutron star with refinement levels inside the star (Sec. V 1);

TOV$_{boost}$ a boosted, nonrotating neutron star crossing refinement levels (Sec. V 2);

TOV$_{mig}$ a migration of an unstable spherical configuration to a stable one crossing refinement levels (Sec. V 3);

RNS$_{BU7}$ a uniformly rotating neutron star with refinement levels inside the star (Sec. V 4);

RNS$_{Kep}$ a neutron star close to the Kepler limit, which is perturbed and finally disrupted crossing refinement levels (Sec. V 5).

For each test we perform simulations for different combinations of the restriction (R), prolongation (P), and correction (C) step, as indicated in Tab. II. The grid parameters are reported in Tab. III. The most important quantity we are focusing on is the rest-mass.

For the simulations we use both the BSSN and the Z4c system. Although no major differences between BSSN and Z4c are observed for what concerns mass conservation, Z4c evolutions show overall smaller violations of the energy-momentum constraints.

1. TOV_{static}

We investigate a spherical star with a gravitational mass of $1.4M_\odot$. The initial data are calculated with a polytropic EOS with $K = 100$ and $\Gamma = 2$. The star is then evolved with the Γ-law EOS. The grid is prepared such that the finest refinement level $l = 4$ is fully contained in the star covering half diameter, and level $l = 3$ ends at the star surface. This is shown in the top panel of Fig. 3, which collects the results. Although at the continuum the solution is trivial (static), in numerical simulations some dynamics is observed due to truncation errors. This is mostly triggered by the artificial atmosphere treatment close to the star surface, and by truncation errors on the refinement levels $l = 2, 3$. Thus, differences in the RPC steps influence the overall dynamics of the system.

The middle and bottom panel of Fig. 3 show the relative error in the rest-mass and its time derivative. The conservative AMR (C step) improves the mass conservation of about ~ 2 orders of magnitude, independently on the particular RP choice. Additionally, we observe differences between the RP combinations. Even using C, the 4th order WENO and Lagrangian RP introduce spurious oscillations in the rest-mass derivative (see green and orange solid lines). In general, using the average R leads to the smallest errors.

These results refer to an atmosphere density $\rho_{atm} = 10^{-9}$. We have experimented with the a2e2 RP setup and an atmosphere density of $\rho_{atm} = 10^{-11}$. The result is shown as a black dashed line in the middle and bottom panel of Fig. 3. A lower atmosphere significantly improves the mass conservation. In this test, the error in the rest-mass derivative related to the C step is about $|dM_b/dt| \sim 10^{-5}$, while the one related to the atmosphere treatment is about $|dM_b/dt| \sim 10^{-f_{atm}\,\rho_{atm}}$. Hence, optimal results can only be obtained with a proper combination of RPC and (f_{atm}, ρ_{atm}).

2. TOV_{boost}

Initial data is prepared using the same star model as Sec. V 1, which is now boosted in the negative x-axis direction[1]. The grid is prepared such that the star is initially entirely covered by the finest refinement level $l = 4$. During motion, the star crosses completely the two finest refinement levels, as shown in Fig. 4 (top panel).

As visible in Fig. 4 (middle and bottom panels) the C step improves mass conservation in most of the cases, but here its effectiveness depends more significantly on the RP choice than in the TOV$_{static}$ test. In particular, the C step is not effective with WENO RP. The a2e2 and a2wz6 schemes perform best, indicating the importance of a conservative R. Similarly to the previous test, we test the role of the atmosphere parameters on the optimal a2e2 setup. Lowering the atmosphere by a factor 100 improves mass conservation by a factor 10 in this case (see dotted black line).

––––––––

[1] We have further tested our implementation by boosting the star in all the directions, and both applying bitant symmetry, i.e. evolving only $z > 0$, and simulating the full numerical domain.

3. TOV_{mig}

We investigate an unstable single neutron star configuration. Initially the central density is $\rho_c = 7.9934 \cdot 10^{-3}$ and the gravitational mass $1.4476 M_\odot$, see e.g. [40]. The star is in an unstable equilibrium, truncation errors trigger a migration to a stable configuration, which involves violent nonlinear oscillations on dynamical timescale. During these expansions and contractions, matter crosses the grid refinement levels. When matter reaches the grid outer boundary some rest-mass falls out of the grid, but typically mass conservation is mostly affected by the interaction between the star low-densities outer layers and the atmosphere. Results are summarized in Fig. 5 for $\rho_{atm} = 10^{-11}$ ($f_{thr} = 10^2$).

We observe the conservative AMR is effective up to times $t \lesssim 400 M_\odot$, that corresponds to ~ 2 bounces of the star core; up to the first bounce the rest-mass conservation improves of about two order of magnitude if the C step is used. At times $t \gtrsim 400$ matter densities $\rho \sim 10^{-5}$ reach outer regions, where the resolution is dropped by a factor of 16 and interaction with atmosphere becomes significant.

Figure 6 summarizes our experiments with atmosphere parameters. Lowering ρ_{thr} by an order of magnitude leads to an improvement of the mass-conservation by approximately one order of magnitude for the beginning of the simulation, while for different ρ_{atm} and the same ρ_{thr} the error stays the same, as expected. Relative rest-mass violation can be minimized up to 10^{-9} using $f_{atm} = 10^{-13}$ and $f_{thr} = 10^2$. One can notice that, if the C step is not applied and the atmosphere is small enough ($\rho_{atm} \lesssim 10^{-10}$), a dramatic mass violation happens as soon as matter crosses the first refinement boundary ($t \sim 100 M_\odot$), see dotted lines in the figure. The same does not happen with the C step. As time advances, rest-mass conservation is progressively corrupted in all the cases due to the drop in resolutions in the outer region reached by the low-density star outer layers bouncing back and forth.

4. RNS_{BU7}

Initial data is a stable uniformly rotating neutron star described by a polytropic EOS with $K = 100$ and $\Gamma = 2$, and with $\rho_c = 1.28 \cdot 10^{-3}$, axes ratio 0.65, and gravitational mass $1.6655 M_\odot$, e.g. [86]. The initial data are computed with the RNS code [87, 88]. The star is evolved with the Γ-law EOS, for about 6 periods. Results are shown in Fig. 7.

As in the previous tests, the C step improves the results in many cases; the best RP setup is a2e2. The l4l4 and l4l4n RP perform equally good at late times. Surprisingly, the nonconservative w4w4n RP is here observed to give good results, and at the end of the simulation, it is comparable to a2e2.

5. RNS_{Kep}

Initial data is a rotating neutron star at the Kepler limit modeled by a polytropic EOS with $K = 100$ and $\Gamma = 2$, and with $\rho_c = 1.444 \cdot 10^{-3}$, axes ratio 0.58, and gravitational mass $1.7498 M_\odot$. The star is evolved with the Γ-law EOS with $\Gamma = 1.9$; the lower polytropic exponent triggers the star expansion with matter crossing several refinement levels.

The left panels of Fig. 8 show how the matter expands along the x-axis and the z-axis over time, i.e. perpendicular and along the symmetry axis. The right panels of the figure show the mass conservation. The best RPC combinations are again a2wz6 and a2e2.

6. Summary of single star tests

Summarizing the results of the single star tests, we find the best mass conservation using the a2e2- scheme, i.e. the average restriction operation and a 2nd order ENO interpolation for the prolongation. The a2e2 simulations show, on average, the smallest dM_b/dt and no artificial oscillations in $1 - M_b(t)/M_b(t = 0)$. The latter are present in at least one test for all other setups than a2e2. We want to mention that the a2e2-scheme was also used in [43] for the computation of a rotating neutron star collapse and showed there the same advantages as outlined here. Additionally, the TOV_{static}, TOV_{boost}, and TOV_{mig} tests suggest that also the artificial atmosphere treatment leads to mass violation. The stability of the simulation improves with higher atmosphere values, but the mass conservation improves for lower atmosphere thresholds. An optimal setup is necessarily a compromise between these two effects. The largest violations of rest-mass conservations are observed in the lowest resolved regions; where the violation becomes independent on the C step and the atmosphere values (i.e. it is mostly due to resolution).

VI.   BNS CONFIGURATIONS & GRID SETUP

For this work we have prepared several BNS irrotational configurations in quasiequilibrium and circular orbits; all the configurations are reported in Tab. IV. Initial data are calculated with the LORENE [89] code.

Our BNS sample spans the EOS sample of Tab. A, and, for each EOS, two mass ratios^2 $q = M_A/M_B = 1, 1.16$ are considered for a fixed total binary mass of $M = M_A + M_B = 2.7$. All EOS support maximal neutron star masses $\gtrsim 2M_\odot$ in agreement with recent observations [90, 91], and the adiabatic speed of sound is $c_s < c$ for a density range up to the maximum density supported by a stable TOV star. The compactnesses of the stars lie within $\mathcal{C} \in [0.129, 0.187]$. The tidal coupling constant spans $\kappa_2^T \in [75, 331]$ (see (23) for the definition). Notice that stiffer EOS have larger κ_2^T, and, for the same EOS and $M = 2.7$, a larger q implies a larger κ_2^T. The initial GW frequency of all binaries is $M\omega_{22}^0 = 0.052$.

Additionally, we computed a $q = 1.5$ and $M = 2.5$ configuration with the MS1b EOS (MS1b-100150). MS1b-100150 has a highly deformable EOS and $\kappa_2^T = 461$. The choice of parameters (EOS, q, M) of this configuration could be considered as "extreme" given the double pulsar population, e.g. [92]. However, the double pulsars sample is rather small to be a significant statistics and the MS1b-100150 parameters are possible.

Some of our $M = 2.7$ configurations have already been investigated in full general relativity in [55, 93]. Thus, the choice of initial data allows us to compare results with the literature. We will also compare with results of [94] employing smooth particles hydrodynamics and conformal flatness, although the evolution method differs and initial data are not prepared in the same way as here.

For the BNS evolutions we use the Z4c scheme [68, 69], and constraint preserving boundary conditions [69, 95]. For all our runs a grid consisting of $L = 7$ refinement levels is used, levels with $l > l^{\text{mv}} = 4$ are dynamically moved. The grid spacing and outer boundary position depends on the employed model and is reported in Tab. IV. For refinement level $l = 0$ we employ the spherical patches, as described in Sec. III; but we do not evolve matter on them. Indicating with r_l the inradius on refinement level $l > 0$, GRHD is evolved up to $r_1 \simeq n \cdot h_1/2$ with resolution h_1, and up to $r_l \sim r_1/2^{l-1}$ with resolutions $h_l = h_1/2^{l-1}$ for $l \geq 1$.

For all binary evolutions we run both the a2e2 and a2e2n RPC schemes. The a2e2 scheme is chosen because of its robustness and best performances in our previous tests; a2e2n is considered in order to assess the effect of the C step in the AMR strategy. We have not considered other combinations due to the computational overhead that they would imply. We set $f_{atm} = 10^{-11}$ and $f_{thr} = 10^2$ for all simulations.

VII.   BNS MERGERS WITH $M = 2.7$ AND $q = 1, 1.16$

We first discuss our results for configurations with mass ratios $q = 1, 1.16$ and a total binary mass $M = 2.7$. We focus on the effect of mass ratio and the EOS on the merger dynamics, ejecta and gravitational waves. Also, we show the use of conservative AMR significantly improves the simulation of the merger remnant. Several results for the configurations of Tab. IV are reported in Tab. V, and collected in Fig. 9, Fig. 10, Fig. 11 and Fig. 12, to which we refer during the discussion.

A.   Effect of EOS and q on merger dynamics

The initial configurations, prepared in quasicircular orbits at the same GW frequency $M\omega_{22}^0 = 0.052$, evolve for about 3 to 5 orbits before merger, depending on the EOS and mass ratio q. Here, the moment of merger is *defined* as the time t_{mrg} corresponding to the peak of the $\ell = m = 2$ multipole of the GW amplitude (see below). Stiffer EOSs give shorter inspiral (less revolutions) and lower dimensionless GW frequency at merger, see $M\omega_{22}^{\text{mrg}}$ in Tab. V. Unequal-mass systems are characterized by slightly shorter inspiral than equal-mass ones and smaller merger frequencies of about $\sim 3\%$. These properties can be understood considering the values of the main ($\ell = 2$) tidal polarizability parameter (tidal coupling constant hereafter) [96],

$$\kappa_2^T = 2 \left(\frac{q^4}{(1+q)^5} \frac{k_2^A}{C_A^5} + \frac{q}{(1+q)^5} \frac{k_2^B}{C_B^5} \right) \, , \tag{23}$$

---

^{2} We define the mass-ratio to be always $q \geq 1$.

where $k_2^{A,B}$ are the $\ell = 2$ dimensionless Love numbers of the individual stars [97–100], in our sample. The results agrees with the analysis of [101]. Essentially, for the same mass, stars with stiff EOS have larger radii than those with soft EOS, and attractive tidal interactions are stronger for larger values of κ_2^T; thus, stiffer EOS binaries merge at lower frequencies. Notice that: (i) $q > 1$ configuration have slightly larger values of κ_2^T than $q = 1$; (ii) in our sample of configurations, EOS effects are typically larger than mass-ratio effects. The late-inspiral dynamics and GWs have been subject of recent work, e.g. [82, 102] and we do not discuss them any further here. In the following we focus on the postmerger dynamics.

The postmerger dynamics has a rich phenomenology depending on the main binary properties: total mass, mass-ratio, EOS and stars' spin (see e.g. [54, 55, 57, 93, 103, 104] for recent work). In the case of irrotational binaries and $M = 2.70 M_\odot$, equal-mass mergers result in a massive differentially rotating compact object, which oscillates violently (see the $\rho_{max} = \max(\rho)$ evolution in Fig. 10 right after merger). The compact object's angular momentum is redistributed from the inner region to outer ones by torque and nonlinear hydrodynamical interaction. The stability of the object depends on the mass, EOS and dissipative processes (see below). Following the literature [105], we define this object as a *hypermassive neutron star* (HMNS), in case its rest-mass is larger than the maximum rest-mass of a stable uniformly rotating star described by the same EOS, or a *supramassive neutron star* (SMNS), in case its rest-mass is smaller. If the object does not exceed the rest mass of a stable TOV-solution, we simply refer to it as *massive neutron star* (MNS). These definitions apply to equilibrium configurations, in particular to cold EOS and axisymmetry, hence, although of common use, they cannot be rigorously applied to the merger remnants. In most cases HMNS are objects that are dynamically unstable and collapse to a black hole on timescales of $\sim 2000 - 10000 M_\odot \sim 10 - 50$ ms; whereas SMNSs are objects that appear stable on those timescales, but may eventually collapse later on due dissipative processes, e.g. loss of angular momentum radiated via GWs. Snapshots of the density distribution and velocities in the orbital plane are presented in Fig. 9; the simulation time is close to the moment of merger.

Three of our $q = 1$ configurations, H4-135135, ALF2-135135, and SLy-135135, merge in a HMNS which collapses to a black hole (BH) within $\tau_{HMNS} \sim 2000 - 5000 \sim 10 - 25$ ms from the merger moment. All these EOSs support approximately the same maximum mass regarding single spherical stars, but the stiffer the EOS, the longer is τ_{HMNS}. This fact can be understood by the following considerations. The range for the tidal coupling constant is $\kappa_2^T \in [75, 331]$, where soft (stiff) EOS binaries correspond to small (large) values in this range. Stiff EOS binaries are gravitationally less bound systems than soft EOS binaries: their binding energy at merger is larger (less negative) as well as the angular momentum. As a result, the HMNS has more angular momentum support at formation. However, the initial angular momentum is not the only factor that determines the lifetime of the HMNS. At formation, the HMNS density in the star core increases, the pressure response depends on the (effective) adiabatic index of the fluid which is different for each EOS. As a result, the HMNS nonlinear oscillations and the efficiency of the angular momentum redistribution depend on the EOS [93]. Stiffer EOSs have larger pressure support against gravity, especially at high densities. Finally, in a more realistic situation than the one simulated here (and on longer timescales), thermal support, angular momentum transport driven by magnetic fields[3] and cooling mechanisms (neutrinos) are expected to play a role. The lifetimes of the HMNS are stated in Tab. V and our results agree with [93] within ± 5 ms.

The merger of MS1-135135, differently from the other $q = 1$ configurations, produces a differentially rotating object that is stable over the whole simulation time, i.e. $6000 M_\odot \sim 30$ ms after merger. Non-rotating stars described by the MS1 EOS can support a maximum rest-mass of $\sim 2.767 M_\odot$. According to the previous definition, we classify the merger remnant for the MS1 models as a MNS. Considering the physics simulated here, we expect that the merger remnant will stabilize via GW emission reaching a uniformly rotating and cold configuration on the characteristic timescale, $\tau_{GW} \sim J/\dot{J} \sim \langle R \rangle^4 / \langle M \rangle^3 \approx 40000 M_\odot \approx 200$ ms.

The unequal-mass $q = 1.16$ configurations H4-125145 and ALF2-125145 have a different merger remnant than the corresponding $q = 1$ configurations. In these cases we find an object stable over $5000 M_\odot \sim 25$ ms, but since the mass is still larger than the supported mass of the uniform rotating model, remnants are HMNSs. We expect these configurations will collapse within $t < \tau_{GW}$. References [55, 93] found that similar configurations with a slightly different thermal component $\Gamma_{th} = 1.8$ form BHs. A similar dynamics as for the MS1-135135 is observed in the merger of MS1-125145, where a stable MNS is produced. The SLy-125145 forms, as in the $q = 1$ case, a black hole, but, following the general trend, the HMNS lifetime is longer.

Due to the unequal mass ratio, the merger remnant is typically more deformed than the corresponding $q = 1$ and strongly non-axisymmetric at formation, see Fig. 9. Unequal-mass binaries have more stable merger remnants than corresponding equal-mass ones (e.g. larger τ_{HMNS}). The $q = 1.16$ HMNS/MNS are characterized by slightly larger radii than the $q = 1$ ones, and a different central density, Fig. 10. Additionally, the mass-ratio has an effect on the

----

[3] We notice the largest simulations with present techniques and resolutions have not properly resolved magnetic field amplification effects [106].

ejecta as we shall see below.

At formation, all the merger remnants show violent oscillations, visible in the evolution of ρ_{max} in Fig. 10. The softer the EOS, the larger are the oscillations, see in particular the SLy panels in the figure. This property reflects the pressure response of the EOS for density jumps around $\rho \gtrsim \rho_2$ (Cf. above and also [93]). The oscillations have a quasi-radial character, and relax either within few radial periods or before the onset of collapse.

In cases with BH formation, the BH masses are of order $2.4 - 2.5\,M_{\odot}$, and the dimensionless BH spin is of the order $0.58 - 0.64$ for all the configurations. The evolution of the BH parameters is presented in Fig. 11 (top and middle panels). These results suggest that, in this scenario, the BH formation and properties are mostly determined by the total mass of the system and depend only weakly on other details. However, uncertainties on these numbers are of the order of $\sim 2\% - 5\%$, and it is difficult to draw precise conclusions.

The final BH is surrounded by an accretion disk of rest-mass $M_{\rm disk} \sim 0.05 - 0.2\,M_{\odot}$, see Tab. V and the bottom panel of Figure 11. The disk geometry is essentially axisymmetric for all the configurations. During the evolution, the maximum density inside the disk decreases from $\sim 10^{-5}$ to $\sim 10^{-7}$. At the moments the BH masses and spins reach their plateaus (late times in our simulations), the dense regions of the disk extend up to distances $\lesssim 30 \sim 45$ km. Lower density, gravitationally bound regions larger than ρ_{atm} extend up to $\sim 100 - 130 \sim 150 - 200$km. The accretion rate is of the order $\dot{M}_{\rm disk} \sim 10^{-8}$.

B. Assessment of conservative AMR

Before continuing the analysis of the physical properties of the merger remnant we discuss here the accuracy improvements due to the numerical algorithm described in Sec. III B. Figure 10 reports result obtained with (solid lines) and without (dashed lines) the C step in the AMR algorithm. The information of the figure is complemented with the entries of Tab. V. For all the configurations the C step is crucial for the simulation accuracy after merger.

Let us first discuss rest-mass conservation. As pointed out in the introduction, the rest-mass can in general increase or decrease. In our BNS simulations we identify two main and competitive causes for the violation of conservation: (i) when fluid crosses refinement boundaries rest-mass tends to *increase*, (ii) the artificial atmosphere treatment tends to *decrease* the rest-mass. Clearly, the C step can improve only violations of type (i).

For most of the configurations the use of the C step leads to an improvement of a factor of ~ 5, except for the MS1-135135-R2 configuration where an improvement by more than a factor of ~ 10 is observed. The only simulation were no significant improvement is observed is SLy-125145-R2, where the violation is $\lesssim 20\%$ from merger to the end of the run.

Overall, the data show some dependence on the EOS. Without C step the mass conservation is in general better for softer EOS; this is probably related to the smaller star deformations. On the contrary, with C step, slightly larger errors are observed for softer EOS. We suggest that this is caused by the influence of numerical viscosity, that, in these runs, is more significant than in the runs without C step due to better overall conservation. Notice that the performance of the conservative AMR algorithm is always better than (or at most comparable to) the corresponding simulations without C step. In [54] we have employed larger grid boxes without C step in an attempt to optimize the performances of the nonconservative AMR for the remnant simulation. In Appendix A we present some experiments along this line showing that conservative AMR is, in general, a better strategy.

Mass-violations influence the behavior and lifetime of the merger remnant, as evident from Fig. 10. We observe systematic shifts in the collapse time of several HMNS although there are no qualitative differences due to the sufficiently high grid resolutions of our runs. For H4-125145 the mass violation in the outer layers in the H4-125145-R2n run determines a slightly different evolution of the MNS and a lower ρ_{max}.

We observe maximal differences of a factor of 3 in the ejecta mass measured on the coarsest level ($l = 1$) between the runs with and without the C step. Figure 10 (bottom panel for each EOS) shows that the differences is larger either shortly after merger time or at later times: no clear trend is identifiable. Thus, low density ejecta remain challenging to simulate even with conservative AMR (as long as nested boxes are used as opposed to local AMR tracking the ejecta). In particular, the artificial atmosphere influence is probably significant: (i) during inspiral we observe some spurious ejecta due to atmosphere fluctuation, and (ii) at late times, when ejecta have expanded into larger radii (coarser resolutions) we expect an effect as the one discussed for the TOV$_{mig}$ test in Sec. V 3.

Differences in the black hole and disk remnant are also observed, see Tab. V and Fig. 11. If the C step is not employed the estimated disk mass $M_{\rm disk}$ changes up to $\sim 0.06 M_{\odot}$. In all configurations the final black hole mass and spin is overestimated when no C step is applied, which is probably related to the increase of the rest-mass visible in the upper panels (for each EOS panel) of Fig. 10 (dashed lines).

Finally, we mention that the GWs calculation during the inspiral is basically not influenced by the use of the C step. This is due to the fact that we have not attempted to refine the grid inside the star during that phase. During

orbital motion the stars stay compact and there is no need of further improving mass conservation. GWs in the post merger reflect the slightly different dynamics, but the characteristic frequencies (see below) are essentially unaffected.

In the following we will discuss exclusively the results obtained with conservative AMR scheme.

C. Ejecta

In this section we discuss the EOS and mass-ratio effect on the dynamical ejecta. A detailed analysis of the dynamical formation of the ejecta will be presented in Sec. VIII.

Figure 10 shows the evolution of the ejecta mass for the various configurations; Tab. V reports the maximum value. Ejecta peaks happen during and shortly after the merger moment; the ejecta rest-masses at this time are about $M_{\mathrm{ejecta}} \sim 10^{-3}\, M_{\odot}$, and in some cases reach $M_{\mathrm{ejecta}} \sim 10^{-2}\, M_{\odot}$.

The amount of ejected material depends on the EOS and on the mass ratio. If $q = 1$ larger ejecta are observed for softer EOS. For a given EOS (but except for SLy EOS), $q = 1.16$ configurations have larger ejecta than $q = 1$ ones. Similarly, the kinetic energy estimate computed according to Eq. (16) is larger for softer EOS and larger q than for stiff ones. Our results for MS1, H4, and ALF2 configurations essentially agree with [55, 94].

We stress that ejecta computations are challenging. At present, mass conservation and artificial atmosphere are the main factors limiting the accuracy. This is evident in the case of SLy configurations. The results in Sec. VII B suggest that the evolution of this soft EOS is less accurate than the others (see also discussion in [55]). We believe this is the reason why M_{ejecta} is larger for SLy-135135 than for SLY-125145. The poor mass conservation in SLY-125145 certainly affects the ejecta calculation. Notice also that a similar setup as SLy-135135 has been evolved in [94]; there, the ejecta mass was estimated to lie in the range between $(4 \cdot 10^{-2}, 6.4 \cdot 10^{-2})$.

D. Gravitational waves

The $\ell = m = 2$ multipoles of the GWs are shown in Fig. 12 for all the configurations. For each EOS, each panel shows the real part of the wave (top) and the instantaneous GW frequency (bottom). The vertical line in each panel marks the moment of merger, defined as the peak of the amplitude $|rh_{22}|$.

The emission from the orbital motion is the characteristic chirping signal, in which frequency and amplitude monotonically increase. At these separations, the dynamics is strongly affected by tidal interactions (parametrized by κ_2^T), and the GWs phase carry information about the EOS. A detailed and accurate semi-analytical modeling of the inspiral up to merger has been given in [102]. The chirp signal ends at the amplitude peak.

After the merger moment, the amplitude instantaneously drops down since the two stars merge in a single body which has, for one instant, a quasispherical geometry [40] (see also the frequency spikes). The postmerger signal is mainly characterized by the nonlinear oscillations of the merger remnant. As discussed above and elsewhere, e.g. [107], the merger remnant can be approximated by a compact star oscillating nonlinearly at the proper frequencies. The $m = 2$ f-mode with frequency f_2 is the most efficient emitter of GWs, and it is strongly excited at formation. Thus, the GW emitted by the HMNS/MNS is dominated by this frequency. Looking at the frequency in Fig. 12, large oscillations are present right after the merger moment and correspond to the very nonlinear phase described in Sec. VII A; softer EOS show larger oscillations. During early stages of the HMNS/MNS evolution, different modes are excited, see e.g. the spectrogram in [54]. Nonlinearity results in mode couplings, the main ones being the combination $f_{\pm} = F \pm f_2$ between the quasiradial mode F and the f_2 [107]. In cases where a MNS is formed (MS1 EOS), the frequency oscillations relax quickly; the power in the $f_{\pm}$ channels decreases, and the frequency essentially settles on the f_2 mode. In cases where a HMNS is formed, the frequency monotonically increases as a result of the star contraction prior to collapse.

Let us finally discuss the GW spectra shown in Fig. 13. The figure includes, for each configuration, the spectrum of the entire signal as a thick line and the spectrum considering only the signal for $t > t_{\mathrm{mrg}}$ as a thin line. Some of the relevant frequencies are marked with bullets: the frequency at the waveform amplitude peak f_{mrg} (triangles), a frequency f_s related to a secondary postmerger peak (circles), and the f_2 frequency corresponding to the main postmerger peak (diamonds). Recently, there has been intense research about the identification and characterization of this postmerger GW spectrum frequencies [55, 93, 107–111]. For most of the configurations, the f_2 frequency is clearly identifiable. Note however the double peak for the MS1 models. The f_2 frequency is smaller for stiffer EOSs; for fixed EOS, $q = 1.16$ configurations have slightly smaller f_2 than $q = 1$. Our f_2 values agree with [55, 94, 112].

The origin of the secondary peak is not well understood. f_s appears mostly related to the very late inspiral phase: several f_s peaks are not present, or strongly suppressed, if the PSD is computed using only times $t > t_{\mathrm{mrg}}$. However, for configuration SLy135135 and H4135135 one can notice a clear secondary peak also in the PSD of the signal at times $t > t_{\mathrm{mrg}}$. We observe that the f_s peaks generated by signals at times $t > t_{\mathrm{mrg}}$ are suppressed for unequal-mass

configurations ($q > 1$). Our values of f_s are in good agreement with the frequencies called f_1 in [112]. Our PSD analysis might be compatible with the interpretation of [111] according to which the peak of the spectrum close to f_s is due to two different effects: the nonlinear mode coupling f_- (that can be extracted clearly using the $t > t_{\mathrm{mrg}}$ signal only), and motion of spiral arms during the last stage of the merger process (but mostly at times $t \lesssim t_{\mathrm{mrg}}$) at a frequency called there f_{spiral}.

VIII. THE MS1B-100150 CONFIGURATION

In this section we consider the evolution of a configuration described by the MS1b EOS [113, 114] with $q = 1.5$ and binary mass $M = 2.5 M_\odot$. The individual stars have masses $M_A = 1.5 M_\odot$ and $M_B = 1.0 M_\odot$. This configuration has (to our knowledge) the largest mass-ratio simulated in numerical relativity. A $q = 1.5$ has been already simulated in [57] for the soft EOS APR, but no gravitational wave signal was computed. The specific MS1b-100150 (Tab. IV) configuration considered here has never been simulated before. We focus on this case study to discuss in some detail the dynamical mechanism that generates the ejecta in the strong field region and the ejecta geometry at their formation. Furthermore, we point out that in the BNS parameter space the combination of stiff EOS and large mass-ratio (and a system with a low mass $\sim 1 M_\odot$ companion) produces a rather peculiar merger remnant in which a MNS is surrounded by a massive and extended accretion disk.

A. Dynamics and Merger remnant

Figure 14 shows a 3D rendering of the density ρ during the merger process at selected times $t \sim 2560, 2957, 3200, 5440$. Both the bound and unbound parts are shown, using an inverse color scale: from yellow to light blue (bound ρ) and from blue to red (unbound ρ). About 1.5 orbit before the moment of merger the stars come in contact; the companion ($M_B = 1 M_\odot$) is very deformed by the tidal field of the primary star ($M_A = 1.5 M_\odot$). We observe the first mass ejection from the low-density outer layers of the companion, $\rho \sim 10^{-8/-9} \sim 10^9$ g cm^{-3} around this time (see the green/blue tail in the top left panel). At later times, the companion is partially disrupted: some material is captured into the primary and forms a hot and differentially rotating core; other material forms a tidal tail, see the top-right and bottom-left panels. Low density material $\rho \lesssim 10^{-7}$ in the outer part of the tidal tail becomes unbound, and it is ejected from these regions during two main episodes. The higher density material, closer to the primary star, expands by centrifugal forces but remains bound. The final merger remnant is composed of a high density hot core surrounded by a thick accretion disk of rest-mass $\sim 0.3 M_\odot$ and of radius $\sim 35 M_\odot \approx 55$km (bottom-right panel). The remnant is not expected to collapse since the total binary rest-mass is smaller than the maximum rest-mass supported by this EOS for spherical configurations (Tab. A).

The rest-mass of the total ejected material is about $M_{\mathrm{ejecta}} \sim 0.03 M_\odot$. The large amount of mass ejected by this configuration offers the possibility to study with enough accuracy the ejecta formation process.

We have checked our results against resolution considering three different grid setups (Tab. VI) and excluding the C step in the AMR algorithm. In Fig. 15 we present the mass conservation and the maximum density evolutions for all setups. The conservative AMR improves results: by the end of the simulation and in the worse case, M_b is conserved up to 0.3% (1.7%) if the C step is (is not) applied. Larger differences in the M_b are observed among different resolutions for the nonconservative AMR runs than for the conservative AMR ones. Interestingly, the central density of the remnant is denser without the C step (bottom panel, compare previous section). Absolute uncertainties in the rest-mass conservation are of order $2.5 \cdot 10^{-3} M_\odot$ by the end of the simulation, and are about a factor 10 smaller of M_{ejecta}.

B. Ejecta formation

Let us discuss the dynamical process at the origin of mass ejection. We identify two main hydrodynamical mechanisms: (i) the torque exerted by the central two-cores structure on the tidal tail; and (ii) shock waves generated in the region between the two cores. Most of the unbound mass is ejected at times close to the moment of merger $t_{\mathrm{mrg}} \sim 2650$ and around the orbital plane with a small opening angle of $\lesssim 15°$. From the first three panels of Fig. 14 one can clearly observe that mass is ejected mostly from the tidal tails primarily of the companion star; the torque mechanism (i) is the dominant one.

In order to further investigate mass ejection, we consider 2D plots of the rest-mass density ρ, velocity v^i, and entropy indicator $\hat{S}$, on the orbital ($x, y, z = 0$) and perpendicular ($x, y = 0, z$) planes, Fig. 16. The color map refers to $\log_{10} \hat{S}$, white contour lines refer to $\rho = (10^{-7}, 10^{-6}, 10^{-5}, 10^{-4}, 10^{-3})$, arrows to the velocity pattern, and regions

delimited by black solid lines highlight unbound material with contour densities $\rho = (10^{-10}, 10^{-9}, 10^{-8}, 10^{-7}, 10^{-6})$ on a logarithmic scale. At time $t \sim 1900$, the revolution/rotation of the cores exerts torque on the low-density outer layers of the companion star. This material gains enough energy to become unbound and the ejection process stars. The ejected material expands with initial velocities $\langle v \rangle_\rho \sim 0.3$ and decompresses. At this times also minor ejecta due to shocks occur (Fig. 16 top left). Between $t \sim t_{\mathrm{mrg}} \sim 2650$ and $t \sim 2900$ mass is also ejected from the tidal tail of the primary star. The entropy has a spiral-like pattern in $\hat{S}$ (Fig. 16); the influence of the thermal pressure component P_{th} is larger in less dense regions. At $t \sim 3000$ we observe another significant event that causes mass ejection. As clear from the bottom panels of Fig. 16, in this case the ejection is triggered by the shock wave generated between the two density maxima of the MNS. The fluid is heated up and driven outward by the thermal pressure (corresponding high entropy regions). The mass is initially ejected in a direction roughly perpendicular to the orbital plane, but it falls back on the orbital plane and acquires angular momentum by torque.

Figure 17 quantifies mass, kinetic energy, and geometry of the ejecta. The rest-mass of the total ejected material is about $M_{\mathrm{ejecta}} \sim 0.03 \, M_\odot$. Notice that, consistently with the discussion in previous sections, the mass decrease is mostly a numerical effect due both to resolution and atmosphere setup. The kinetic energy of the ejecta is $T_{\mathrm{ejecta}} \sim 3.2 \cdot 10^{-4} \sim 2.9 \cdot 10^{50}$ erg. Regarding the geometry, lower panel of Fig. 17, we observe that mass expands inside the orbital plane more rapidly than perpendicular to it. The analysis of the $\langle \rho \rangle$ and $\langle z \rangle$ curves suggests that the ejecta extends mainly around the equatorial plane with an opening angle of $\theta \sim \arctan z/\rho \sim 10°$ (compare Eq.(19) and (20)). On large spatial scales, the geometry is anisotropic.

The basic mechanisms (i) and (ii) identified in this case study are rather general and at the origin of mass ejection also in other configurations. Thus, the geometrical and kinematic properties of dynamical ejecta at their formation described here are expected to be representative, at least at a qualitative level (see also [55, 56]).

Clearly, configuration details, in particular the EOS and mass ratio, may lead to quantitative differences. The inclusion of microphysical aspects, neutrinos and magnetic fields may change the picture [56], but because the mechanisms producing mass ejection described here operate on very short timescales of a few milliseconds during the merger, we expect differences only on longer timescales.

IX. CONCLUSION

In this work, we have investigated the merger remnant of neutron star binaries using ab initio numerical relativity simulations which employ a conservative algorithm for the adaptive mesh refinement (AMR) technique. Our results are summarized in the following.

(i) We have presented a new implementation of the Berger-Collela mesh refinement algorithm in the BAM code. The algorithm has been extensively tested in single star spacetimes focusing on its performances when combined with different reconstruction and prolongation operators and a standard artificial atmosphere treatment for the vacuum regions.

The use of a correction step in the AMR algorithm significantly improves rest-mass conservation. In all our tests we found an improvement of at least a factor of ~ 10 up to a factor of $\sim 10^5$. However, mass conservation depends also on the atmosphere parameters. Typically, smaller atmosphere levels led to smaller violations. The choice of the restriction/prolongation operators can be delicate as well. The best mass conservation was obtained, for most of the cases, using the average restriction and a 2nd-order ENO prolongation.

(ii) We have applied the conservative AMR in neutron star mergers simulations and focused on the study of the merger remnant. We considered initial binary configurations with different EOS, binary mass $2.7 \, M_\odot$, and two mass ratios $q = 1, 1.16$. Very similar simulations where performed in [55, 93]. We studied the dependence of the merger outcome as a function of the EOS and q. For $M = 2.7 \, M_\odot$ a massive differentially rotating object is produced, the properties of which mostly dependent on the EOS. Stiffer EOSs produce more stable remnants, and eventually stable objects (MNS) in cases the total rest-mass is less than the one supported by a spherical configuration with the same EOS. Softer EOSs produce a hyper-massive neutron star (HMNS) which collapses on dynamical timescales. The HMNS collapses to a black hole with mass $M_{\mathrm{BH}} \sim 2.4 - 2.5 \, M_\odot$ and dimensionless spin $\sim 0.58 - 0.64$. An accretion disk of rest-mass $M_{\mathrm{disk}} \sim 0.05 - 0.2 \, M_\odot$ and a radius of ~ 40 km is observed.

All the simulations were computed with and without conservative AMR. The conservative algorithm typically improved rest-mass conservation by a factor of ~ 5, depending on the specific resolution and binary configuration. At the resolutions employed, rest-mass violations can lead to inaccuracies in the collapse time, and to systematic errors regarding the mass of the accretion disk, and the black hole mass/spin. Differences in the ejecta are also observed, although no general trend could be identified. Our results indicate that the use of conservative AMR is desirable and recommended in postmerger simulations.

We studied dynamical mass ejection and found that a total rest-mass of about $M_{\mathrm{ejecta}} \sim 10^{-3} - 10^{-2} \, M_\odot$ becomes unbound during merger with kinetic energy $T_{\mathrm{ejecta}} \sim 10^{-4} \sim 10^{50}$ erg. The amount of ejected material depends on

the EOS and on the mass ratio q. For $q = 1$ larger ejecta are observed for softer EOSs. For a given EOS, larger q gives larger ejecta. Overall, our results agree with those of [55, 94]. Even with conservative AMR the computation of ejecta is challenging for numerical relativity grid-based codes, at least when the moving-box algorithm with nested boxes centered on the stars is used. Conceivably, a local AMR strategy that tracks the ejecta could be advantageous. In order to obtain the best performance one needs to carefully set and experiment with the atmosphere parameters.

(iii) As a new application we have performed, for the first time, a simulation of a $q = 1.5$ configuration with the stiff EOS MS1b. Mass-ratio $q = 1.5$ is the largest mass ratio simulated so far in numerical relativity, simulated in [57] for a very soft EOS. Here, we considered the very stiff EOS MS1b; the two stars have masses $1.00 M_\odot$ and $1.50 M_\odot$.

During merger the companion (less massive star) is strongly deformed by the tidal field of the primary and develops a tidal tail. The final merger remnant is composed by a high density hot core surrounded by a thick accretion disk of rest-mass $\sim 0.3 M_\odot$ and of radius $\sim 35 M_\odot \sim 55$km (see Fig. 14). The remnant is not expected to collapse since the total binary rest-mass is smaller than the maximum rest-mass supported by a spherical configuration.

The MS1b-100150 configuration has the largest amount of ejected rest-mass in our sample, $M_{\rm ejecta} \sim 0.03 M_\odot$. Ejecta mainly originate from the tidal tail; density layers of order $\rho \sim 10^{-9} - 10^{-7} \sim 10^8 - 10^{10}$ g cm^{-3} are accelerated up to $v \sim 0.3$ and become unbound. Most of the unbound mass is ejected in a time window of a few milliseconds around the moment of merger, $t_{\rm mrg}$. We identified two mechanisms for the ejecta emission: (i) the torque exerted by the central two-cores structure on the tidal tail; and (ii) shocks waves generated between the two MNS cores. The geometry of the emission is anisotropic. Although configuration details may lead to some quantitative differences, we suggest that our qualitative picture is rather robust and captures accurately the short timescale dynamics of the ejecta.

We believe configurations like MS1b-100150 are astrophysically plausible and potentially relevant for strong electromagnetic (and neutrino) signals. They should be investigated in the future in more detail including magnetic fields, microphysics and radiation transport in the simulations.

Acknowledgments

Appendix A: Box-sizes in BNS simulations

In this appendix we investigate the influence of the box settings on the HMNS dynamics. In [54] we have experimented with the box sizes in an attempt of improving rest-mass conservation in the postmerger phase without using a conservative algorithm. We briefly compare here the two approaches.

Focusing on SLy-125145-R2, we consider runs with the different grid setting of Tab. IV. In the grid setup R2[cn]1 and R2[cn]2, the number of points per direction is kept fixed but the resolution is slightly changed in order to increase the box size. Changing the resolution has two competitive effects. On the one hand, the merger remnant is better resolved with a smaller grid spacing; but on the other hand the box size decreases and more matter can crosses refinement boundaries.

Figure 18 shows the central density and the gravitational wave signal. If no C step is employed, we observe a large shift ($\sim 700 M_\odot \sim 3.5$ ms) in the collapse time. As an effect of the non-conservative AMR, the total mass increases and the system collapses earlier. In case the C step is applied a smaller shift of about $\sim 300 M_\odot \sim 1.5$ ms is observed. This is possibly due to a similar effect as above, but of reduced magnitude and possibly due to the different resolution. No visible differences are observed in the GW signal instead.

Increasing the box size while maintaining the same resolution increases the computational cost significantly, $\sim n^3$. On the other hand the computational overhead due to the C step amount to a maximum of 10% in simulation speed, in the cases where the mask for the child and parent cells have to be computed often. We conclude the conservative

AMR is a better approach.

----

[1] D. Eichler, M. Livio, T. Piran, and D. N. Schramm, Nature **340**, 126 (1989).
[2] N. Andersson, J. Baker, K. Belczynski, S. Bernuzzi, E. Berti, et al., Class.Quant.Grav. **30**, 193002 (2013), 1305.0816.
[3] S. Rosswog (2015), 1501.02081.
[4] R. Hulse and J. Taylor, Astrophys.J. **195**, L51 (1975).
[5] J. Weisberg, D. Nice, and J. Taylor, Astrophys.J. **722**, 1030 (2010), 1011.0718.
[6] M. Burgay, N. D'Amico, A. Possenti, R. Manchester, A. Lyne, et al., Nature **426**, 531 (2003), astro-ph/0312071.
[7] A. Lyne, M. Burgay, M. Kramer, A. Possenti, R. Manchester, et al., Science **303**, 1153 (2004), astro-ph/0401086.
[8] M. Kramer, I. H. Stairs, R. Manchester, M. McLaughlin, A. Lyne, et al., Science **314**, 97 (2006), astro-ph/0609417.
[9] LIGO - Laser Interferometer Gravitational Wave Observatory, URL {http://www.ligo.caltech.edu/}.
[10] Virgo/EGO, European Gravitational Observatory, URL {http://www.ego-gw.it/}.
[11] J. Abadie et al. (LIGO Scientific Collaboration, Virgo Collaboration), Class.Quant.Grav. **27**, 173001 (2010), 1003.2480.
[12] J. Aasi et al. (LIGO Scientific Collaboration, Virgo Collaboration) (2013), 1304.0670.
[13] B. Metzger and E. Berger, Astrophys.J. **746**, 48 (2012), 1108.6056.
[14] B. Paczynski, Astrophys. J. **308**, L43 (1986).
[15] J. M. Lattimer and D. N. Schramm, apjl **192**, L145 (1974).
[16] S. Rosswog, M. Liebendoerfer, F. Thielemann, M. Davies, W. Benz, et al., Astron.Astrophys. **341**, 499 (1999), astro-ph/9811367.
[17] S. Goriely, A. Bauswein, and H.-T. Janka (2011), 1107.0899.
[18] L.-X. Li and B. Paczynski, Astrophys.J. **507**, L59 (1998), astro-ph/9807272.
[19] N. Tanvir, A. Levan, A. Fruchter, J. Hjorth, K. Wiersema, et al., Nature **500**, 547 (2013), 1306.4971.
[20] B. Yang, Z.-P. Jin, X. Li, S. Covino, X.-Z. Zheng, et al. (2015), 1503.07761.
[21] B. Metzger, G. Martinez-Pinedo, S. Darbha, E. Quataert, A. Arcones, et al., Mon.Not.Roy.Astron.Soc. **406**, 2650 (2010), 1001.5029.
[22] E. Waxman, New J.Phys. **6**, 140 (2004).
[23] C. D. Dermer and J. M. Holmes, Astrophys.J. **628**, L21 (2005), astro-ph/0504158.
[24] J. N. Bahcall and P. Meszaros, Phys.Rev.Lett. **85**, 1362 (2000), hep-ph/0004019.
[25] L. Dessart, C. Ott, A. Burrows, S. Rosswog, and E. Livne (2008), 0806.4380.
[26] A. Perego, S. Rosswog, R. Cabezon, O. Korobkin, R. Kaeppeli, et al., Mon.Not.Roy.Astron.Soc. **443**, 3134 (2014), 1405.6730.
[27] J. A. Faber and F. A. Rasio, Living Rev.Rel. **15**, 8 (2012), 1204.3858.
[28] M. J. Berger and J. Oliger, J.Comput.Phys. **53**, 484 (1984).
[29] M. W. Choptuik, in *Frontiers in Numerical Relativity*, edited by C. Evans, L. Finn, and D. Hobill (Cambridge University Press, Cambridge, England, 1989), pp. 206–221.
[30] B. Brügmann, Phys. Rev. **D54**, 7361 (1996), gr-qc/9608050.
[31] E. Schnetter, S. H. Hawley, and I. Hawke, Class.Quant.Grav. **21**, 1465 (2004), gr-qc/0310042.
[32] E. Evans, S. Iyer, E. Schnetter, W.-M. Suen, J. Tao, et al., Phys.Rev. **D71**, 081301 (2005), gr-qc/0501066.
[33] B. Brügmann, J. A. Gonzalez, M. Hannam, S. Husa, U. Sperhake, et al., Phys.Rev. **D77**, 024027 (2008), gr-qc/0610128.
[34] B. Brügmann, Int. J. Mod. Phys. **D8**, 85 (1999), gr-qc/9708035.
[35] J. G. Baker, J. Centrella, D.-I. Choi, M. Koppitz, and J. van Meter, Phys. Rev. Lett. **96**, 111102 (2006), gr-qc/0511103.
[36] M. Campanelli, C. O. Lousto, P. Marronetti, and Y. Zlochower, Phys. Rev. Lett. **96**, 111101 (2006), gr-qc/0511048.
[37] M. Shibata and K. Uryu, Phys. Rev. **D61**, 064001 (2000), gr-qc/9911058.
[38] M. Shibata, K. Taniguchi, and K. Uryu, Phys. Rev. **D71**, 084021 (2005), gr-qc/0503119.
[39] L. Baiotti, B. Giacomazzo, and L. Rezzolla, Phys. Rev. **D78**, 084033 (2008), 0804.0594.
[40] M. Thierfelder, S. Bernuzzi, and B. Brügmann, Phys.Rev. **D84**, 044012 (2011), 1104.4751.
[41] L. Baiotti, I. Hawke, P. J. Montero, F. Loffler, L. Rezzolla, et al., Phys.Rev. **D71**, 024035 (2005), gr-qc/0403029.
[42] C. Reisswig, R. Haas, C. Ott, E. Abdikamalov, P. Mösta, et al., Phys.Rev. **D87**, 064023 (2013), 1212.1191.
[43] T. Dietrich and S. Bernuzzi, Phys.Rev. **D91**, 044039 (2015), 1412.5499.
[44] C. D. Ott, A. Burrows, E. Livne, and R. Walder, Astrophys.J. **600**, 834 (2004), astro-ph/0307472.
[45] M. Shibata, Y. T. Liu, S. L. Shapiro, and B. C. Stephens, Phys. Rev. **D74**, 104026 (2006), astro-ph/0610840.
[46] M. J. Berger and P. Colella, Journal of Computational Physics **82**, 64 (1989).
[47] W. E. East, F. Pretorius, and B. C. Stephens, Phys.Rev. **D85**, 124010 (2012), 1112.3094.
[48] B. C. Stephens, W. E. East, and F. Pretorius, Astrophys.J. **737**, L5 (2011), 1105.3175.
[49] W. E. East and F. Pretorius, Astrophys.J. **760**, L4 (2012), 1208.5279.
[50] C. D. Ott, E. Abdikamalov, P. Msta, R. Haas, S. Drasco, et al., Astrophys.J. **768**, 115 (2013), 1210.6674.
[51] C. Reisswig, C. Ott, E. Abdikamalov, R. Haas, P. Moesta, et al., Phys.Rev.Lett. **111**, 151101 (2013), 1304.7787.
[52] E. Abdikamalov, C. Ott, D. Radice, L. Roberts, R. Haas, et al. (2014), 1409.7078.
[53] T. Dietrich and B. Brügmann, J.Phys.Conf.Ser. **490**, 012155 (2014), 1403.5746.
[54] S. Bernuzzi, T. Dietrich, W. Tichy, and B. Brügmann, Phys.Rev. **D89**, 104021 (2014), 1311.4443.

[55] K. Hotokezaka, K. Kiuchi, K. Kyutoku, H. Okawa, Y.-i. Sekiguchi, et al., Phys.Rev. **D87**, 024001 (2013), 1212.0905.
[56] Y. Sekiguchi, K. Kiuchi, K. Kyutoku, and M. Shibata (2015), 1502.06660.
[57] M. Shibata and K. Taniguchi, Phys.Rev. **D73**, 064027 (2006), astro-ph/0603145.
[58] V. Hambaryan, V. Suleimanov, A. D. Schwope, R. Neuhäuser, K. Werner, and A. Y. Potekhin, aap **53**, A74 (2011).
[59] V. Hambaryan, R. Neuhäuser, V. Suleimanov, and K. Werner, Journal of Physics Conference Series **496**, 012015 (2014).
[60] E. Gourgoulhon (2007), gr-qc/0703035.
[61] J. A. Font, Living Rev. Rel. **11**, 7 (2007).
[62] L. Rezzolla and O. Zanotti, *Relativistic hydrodynamics* (Oxford University Press, 2013).
[63] J. S. Read, B. D. Lackey, B. J. Owen, and J. L. Friedman, Phys. Rev. **D79**, 124032 (2009), 0812.2163.
[64] A. Bauswein, H. T. Janka, and R. Oechslin (2010), 1006.3315.
[65] T. Nakamura, K. Oohara, and Y. Kojima, Prog. Theor. Phys. Suppl. **90**, 1 (1987).
[66] M. Shibata and T. Nakamura, Phys. Rev. **D52**, 5428 (1995).
[67] T. W. Baumgarte and S. L. Shapiro, Phys. Rev. **D59**, 024007 (1999), gr-qc/9810065.
[68] S. Bernuzzi and D. Hilditch, Phys. Rev. **D81**, 084003 (2010), 0912.2920.
[69] D. Hilditch, S. Bernuzzi, M. Thierfelder, Z. Cao, W. Tichy, et al., Phys. Rev. **D88**, 084057 (2013), 1212.2901.
[70] C. Bona, J. Massó, E. Seidel, and J. Stela, Phys. Rev. Lett. **75**, 600 (1995), gr-qc/9412071.
[71] M. Alcubierre, B. Brügmann, P. Diener, M. Koppitz, D. Pollney, et al., Phys.Rev. **D67**, 084023 (2003), gr-qc/0206072.
[72] J. R. van Meter, J. G. Baker, M. Koppitz, and D.-I. Choi, Phys. Rev. **D73**, 124011 (2006), gr-qc/0605030.
[73] M. Thierfelder, S. Bernuzzi, D. Hilditch, B. Brügmann, and L. Rezzolla, Phys.Rev. **D83**, 064022 (2011), 1012.3703.
[74] A. Staley, T. Baumgarte, J. Brown, B. Farris, and S. Shapiro, Class.Quant.Grav. **29**, 015003 (2012), 1109.0546.
[75] D. Hilditch, T. W. Baumgarte, A. Weyhausen, T. Dietrich, B. Brügmann, et al., Phys.Rev. **D88**, 103009 (2013), 1309.5008.
[76] B. Brügmann, W. Tichy, and N. Jansen, Phys. Rev. Lett. **92**, 211101 (2004), gr-qc/0312112.
[77] T. Yamamoto, M. Shibata, and K. Taniguchi, Phys. Rev. **D78**, 064054 (2008), 0806.4007.
[78] C. Ronchi, R. Iacono, and P. Paolucci, Journal of Computational Physics **124**, 93 (1996), ISSN 0021-9991, URL http://www.sciencedirect.com/science/article/pii/S0021999196900479.
[79] J. Thornburg, Class.Quant.Grav. **21**, 3665 (2004), gr-qc/0404059.
[80] D. Pollney, C. Reisswig, E. Schnetter, N. Dorband, and P. Diener, Phys. Rev. **D83**, 044045 (2011), 0910.3803.
[81] R. Borges, M. Carmona, B. Costa, and W. S. Don, Journal of Computational Physics **227**, 3191 (2008).
[82] S. Bernuzzi, A. Nagar, M. Thierfelder, and B. Brügmann, Phys.Rev. **D86**, 044030 (2012), 1205.3403.
[83] A. Harten, Journal of Computational Physics **83**, 148 (1989), ISSN 0021-9991.
[84] G. Jiang, J. Comp. Phys. **126**, 202 (1996).
[85] C. Reisswig and D. Pollney, Class.Quant.Grav. **28**, 195015 (2011), 1006.1632.
[86] H. Dimmelmeier, N. Stergioulas, and J. A. Font, Mon. Not. Roy. Astron. Soc. **368**, 1609 (2006), astro-ph/0511394.
[87] N. Stergioulas and J. L. Friedman, Astrophys. J. **444**, 306 (1995), astro-ph/9411032.
[88] T. Nozawa, N. Stergioulas, E. Gourgoulhon, and Y. Eriguchi, Astron. Astrophys. Suppl. Ser. **132**, 431 (1998), gr-qc/9804048.
[89] E. Gourgoulhon, P. Grandclément, J.-A. Marck, J. Novak, and K. Taniguchi, http://www.lorene.obspm.fr.
[90] P. Demorest, T. Pennucci, S. Ransom, M. Roberts, and J. Hessels, Nature **467**, 1081 (2010), 1010.5788.
[91] J. Antoniadis, P. C. Freire, N. Wex, T. M. Tauris, R. S. Lynch, et al., Science **340**, 6131 (2013), 1304.6875.
[92] B. Kiziltan, A. Kottas, M. De Yoreo, and S. E. Thorsett, Astrophys.J. **778**, 66 (2013), 1309.6635.
[93] K. Hotokezaka, K. Kiuchi, K. Kyutoku, T. Muranushi, Y.-i. Sekiguchi, et al. (2013), 1307.5888.
[94] A. Bauswein, S. Goriely, and H.-T. Janka, Astrophys.J. **773**, 78 (2013), 1302.6530.
[95] M. Ruiz, D. Hilditch, and S. Bernuzzi, Phys. Rev. **D83**, 024025 (2011), 1010.0523.
[96] T. Damour and A. Nagar, Phys. Rev. **D81**, 084016 (2010), 0911.5041.
[97] T. Hinderer, Astrophys.J. **677**, 1216 (2008), 0711.2420.
[98] T. Damour and A. Nagar, Phys. Rev. **D80**, 084035 (2009), 0906.0096.
[99] T. Binnington and E. Poisson, Phys. Rev. **D80**, 084018 (2009), 0906.1366.
[100] T. Hinderer, B. D. Lackey, R. N. Lang, and J. S. Read, Phys. Rev. **D81**, 123016 (2010), 0911.3535.
[101] S. Bernuzzi, A. Nagar, S. Balmelli, T. Dietrich, and M. Ujevic, Phys.Rev.Lett. **112**, 201101 (2014), 1402.6244.
[102] S. Bernuzzi, A. Nagar, T. Dietrich, and T. Damour (2014), 1412.4553.
[103] M. Shibata, Y. Suwa, K. Kiuchi, and K. Ioka (2011), 1105.3302.
[104] W. Kastaun and F. Galeazzi (2014), 1411.7975.
[105] T. W. Baumgarte, S. L. Shapiro, and M. Shibata, Astrophys. J. **528**, L29 (2000), astro-ph/9910565.
[106] K. Kiuchi, K. Kyutoku, Y. Sekiguchi, M. Shibata, and T. Wada, Phys.Rev. **D90**, 041502 (2014), 1407.2660.
[107] N. Stergioulas, A. Bauswein, K. Zagkouris, and H.-T. Janka (2011), 1105.0368.
[108] A. Bauswein and H.-T. Janka, Phys.Rev.Lett. **108**, 011101 (2012), 1106.1616.
[109] A. Bauswein, N. Stergioulas, and H. T. Janka (2014), 1403.5301.
[110] K. Takami, L. Rezzolla, and L. Baiotti, Phys.Rev.Lett. **113**, 091104 (2014), 1403.5672.
[111] A. Bauswein and N. Stergioulas (2015), 1502.03176.
[112] K. Takami, L. Rezzolla, and L. Baiotti, Phys.Rev. **D91**, 064001 (2015), 1412.3240.
[113] H. Müller and B. D. Serot, Nucl. Phys. **A606**, 508 (1996), nucl-th/9603037.
[114] J. Lattimer and M. Prakash, Astrophys.J. **550**, 426 (2001), astro-ph/0002232.

Figures
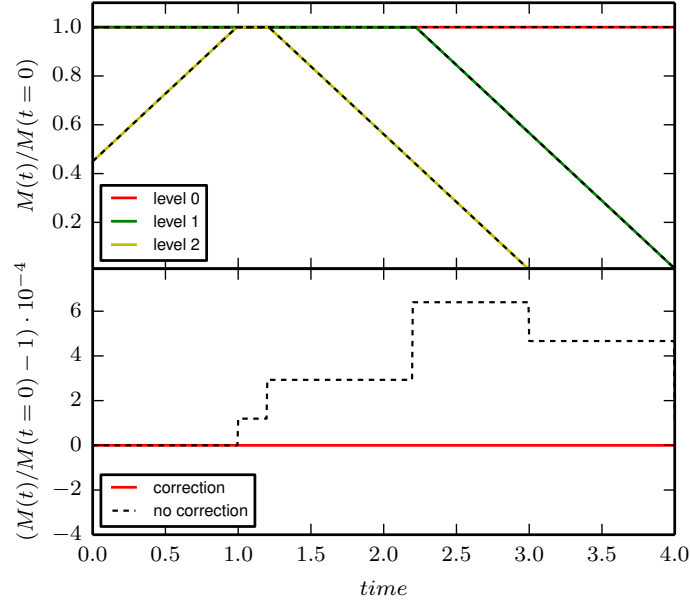
FIG. 1: Conservative mesh refinement for the 1D advection equation. The plot compares the mass conservation for a discontinuous profile flowing into two refinement levels in the two cases in which the mass correction is applied or not. Top: mass evolution on the three levels for the non-conservative (dashed lines) and the conservative method (solid). Bottom: evolution of mass relative error on the the coarsest level for the non-conservative (dashed lines) and the conservative method (solid). The solid red line is at round-off level.
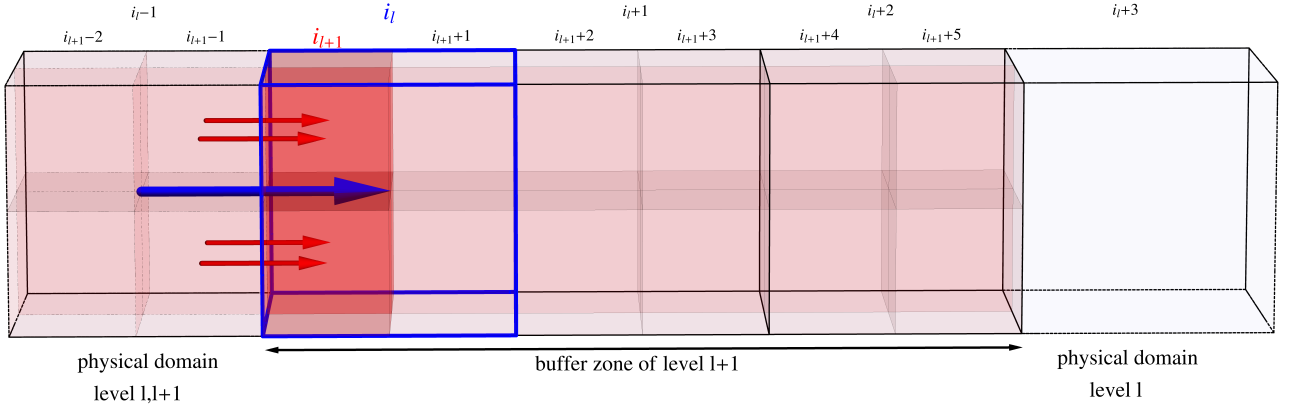
FIG. 2: Sketch of the mesh-refinement. We focus on the buffer region along the positive x-direction. Light red cells refer to the buffer region between level l and level $l+1$. We employ six buffer points in level $l+1$. Prolongation (P) and correction (C) steps take place in this region. The *parent* cell is visualized by the blue bounding box, while the *child* cells are colored dark red. The fluxes across the physical domain and the refinement buffer zone are visualized with arrows. The parent cell (level l) receives the correction after level $l+1$ has been evolved.
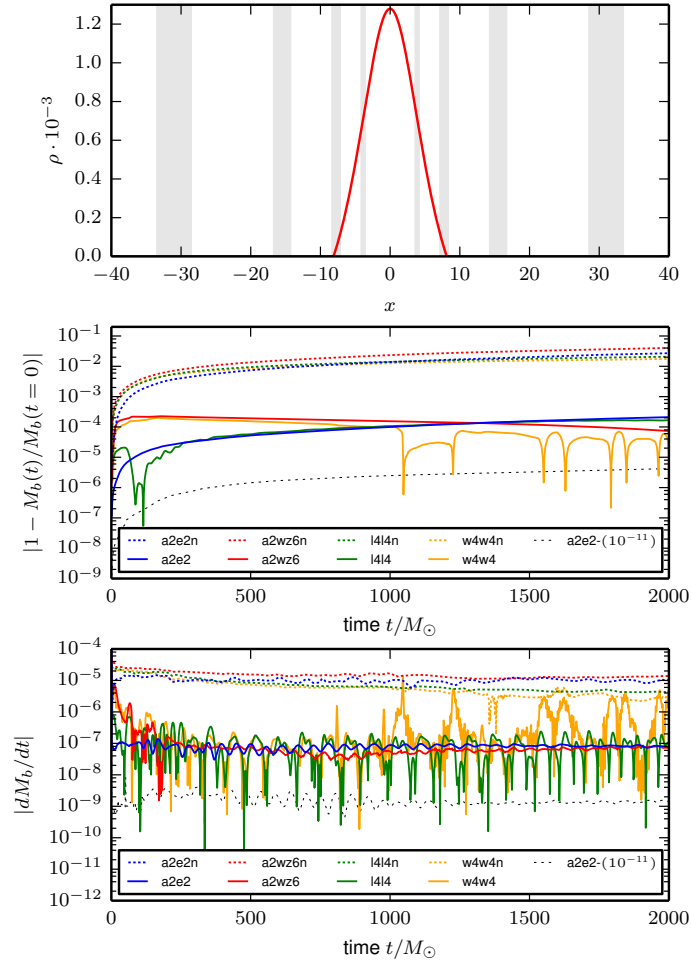
FIG. 3: Results of the TOV_{static} test. Top: Initial density profile of TOV_{static} test along the x-axis. The buffer zones of the refinement levels are shaded in gray. Middle: The relative rest-mass change $|1 - \frac{M_b(t)}{M_b(t=0)}|$ for different RPC combinations with an atmosphere of $f_{atm} = 10^{-9}, f_{thr} = 10^2$ and additionally for a2e2 with an atmosphere of $f_{atm} = 10^{-9}, f_{thr} = 10^2$ (black dashed line).

Bottom: The time derivative of the rest-mass.
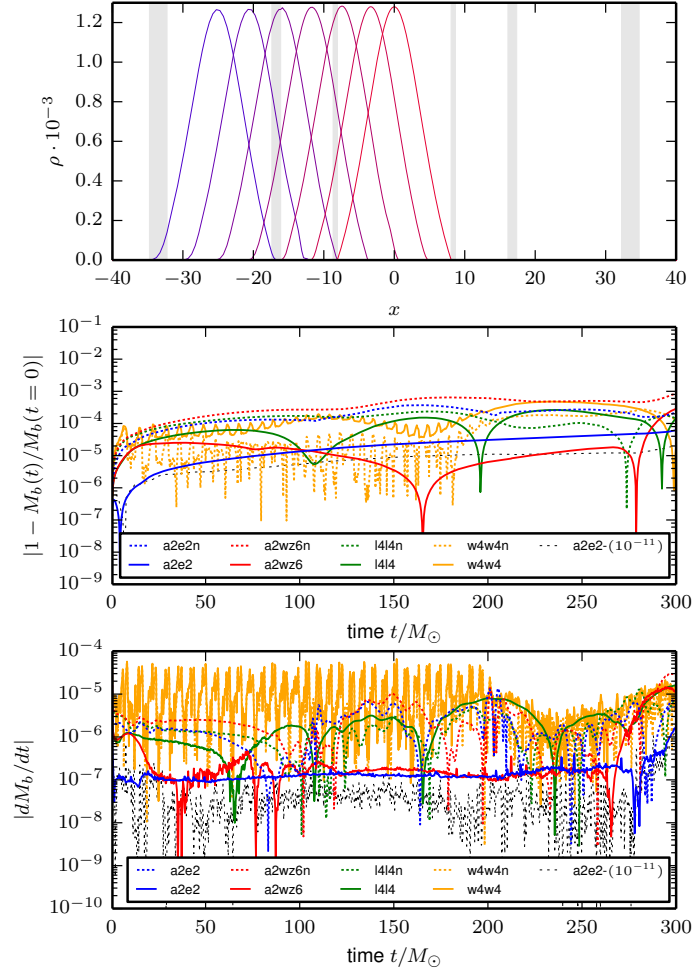
FIG. 4: Results of the TOV$_{boost}$ test. Top: Evolution of the density profile along the x-axis; the profiles correspond to times $t = 0, 50, 100, 150, 200, 250, 300 M_{\odot}$, and boost in the negative x direction. The buffer zones of the refinement levels are shaded in gray. Middle: The relative rest-mass change for different RPC combinations with an atmosphere of $f_{atm} = 10^{-9}, f_{thr} = 10^2$ and additionally for a2e2 with an atmosphere of $f_{atm} = 10^{-9}, f_{thr} = 10^2$ (black dashed line).
Bottom: The time derivative of the rest-mass.
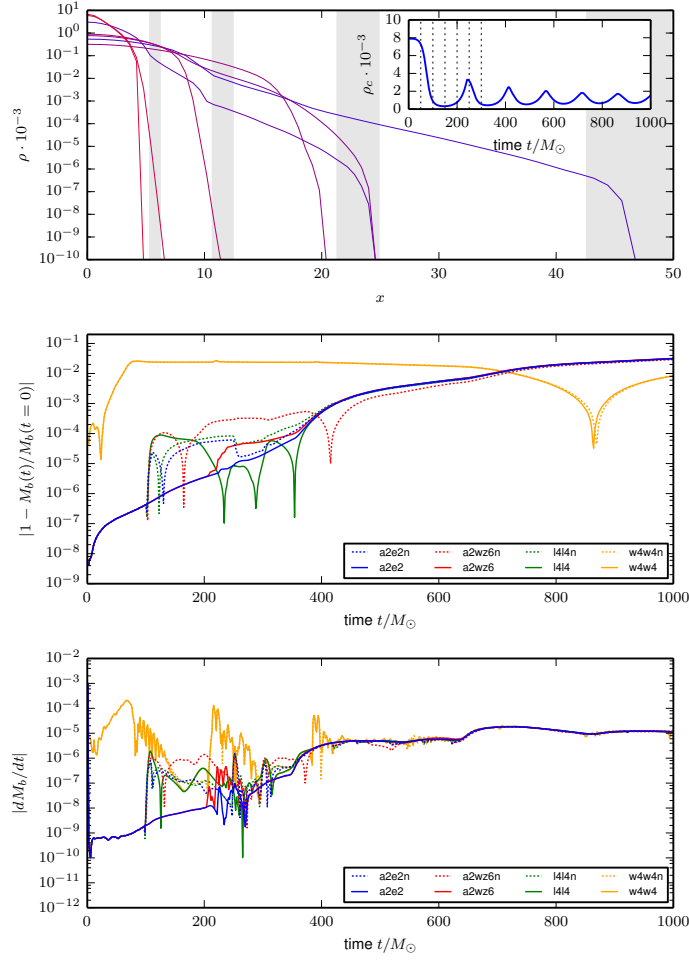
FIG. 5: Results of the TOV_{mig} test. Top: Evolution of the density profile along the x-axis; the profiles correspond to times $t = 0, 50, 100, 150, 200, 250, 300 M_\odot$. The buffer zones of the refinement levels are shaded in gray. The star first expands reaching $r \sim 50$, then contracts, then bounces back and forth several times. The inset shows the time evolution of the central density. The vertical dashed lines refer to the times shown in this panel. Middle: The relative rest-mass change for different RPC combinations. Bottom: The time derivative of the rest-mass.
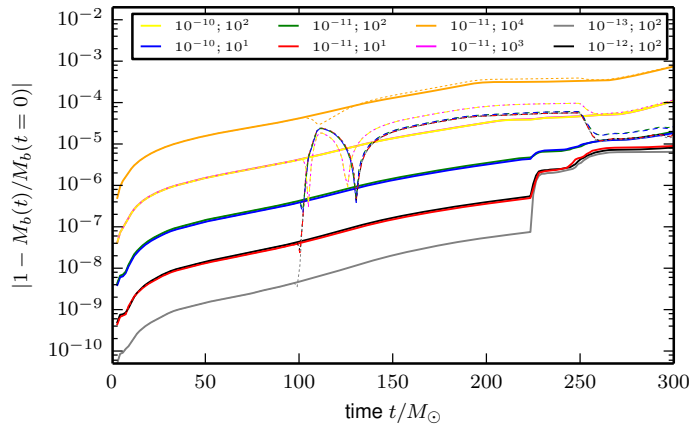
FIG. 6: Results of the TOV_{mig} test: influence of the atmosphere parameters. In the legend, the first number represents f_{atm}, the second number f_{thr}. Solid lines correspond to simulations with a2e2 RPC; dotted lines to simulations with a2e2n RPC, i.e. without C step.
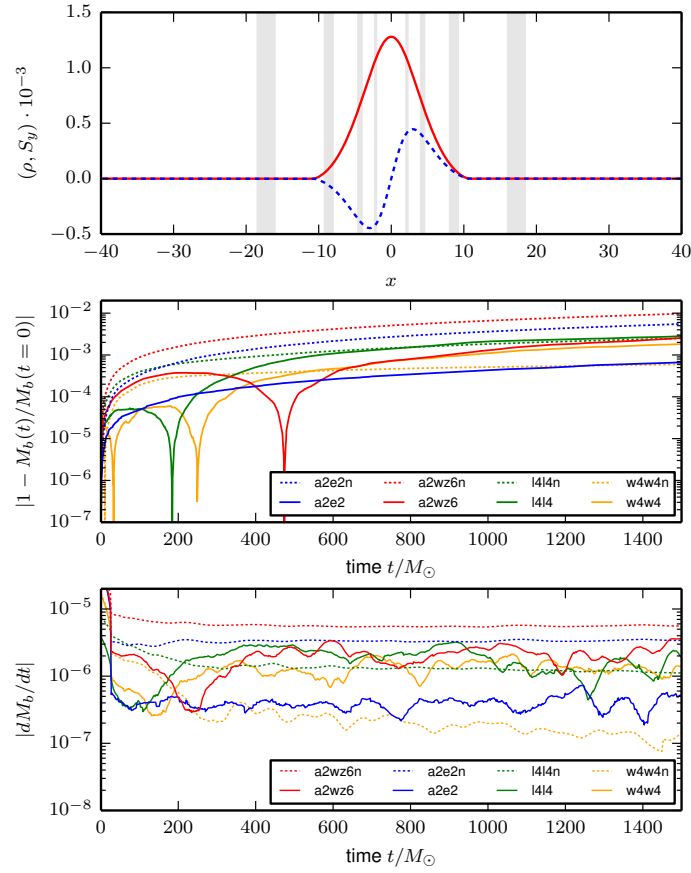
FIG. 7: Results of the RNS$_{BU7}$ test. Top: Density profile (red) and momentum density (blue) along the x-axis Middle: Relative rest-mass change for different RPC combinations. Bottom: The time derivative of the rest-mass.
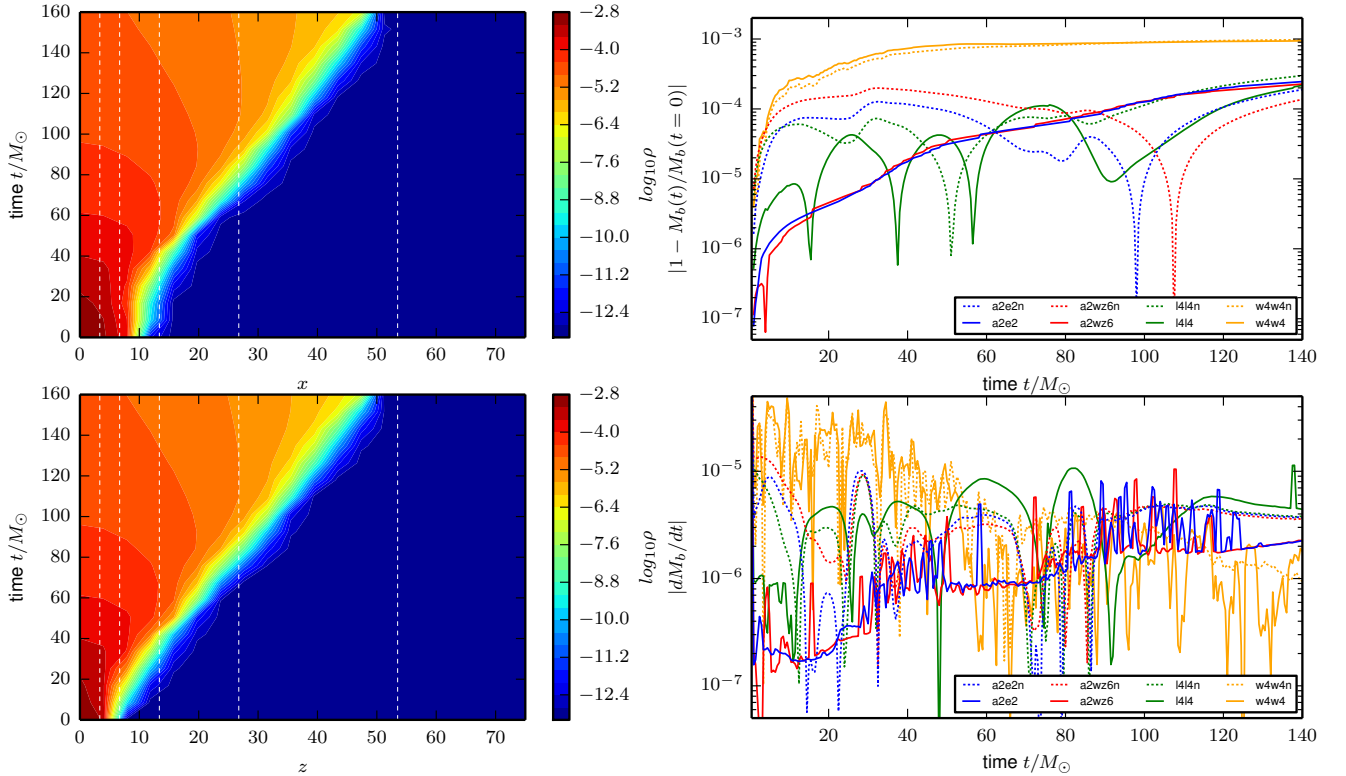
FIG. 8: Results of the RNS$_{\text{Kep}}$ test. Left: Density evolution along directions x and z. Right: The relative rest-mass change and rest-mass time-derivative for different RPC combinations.
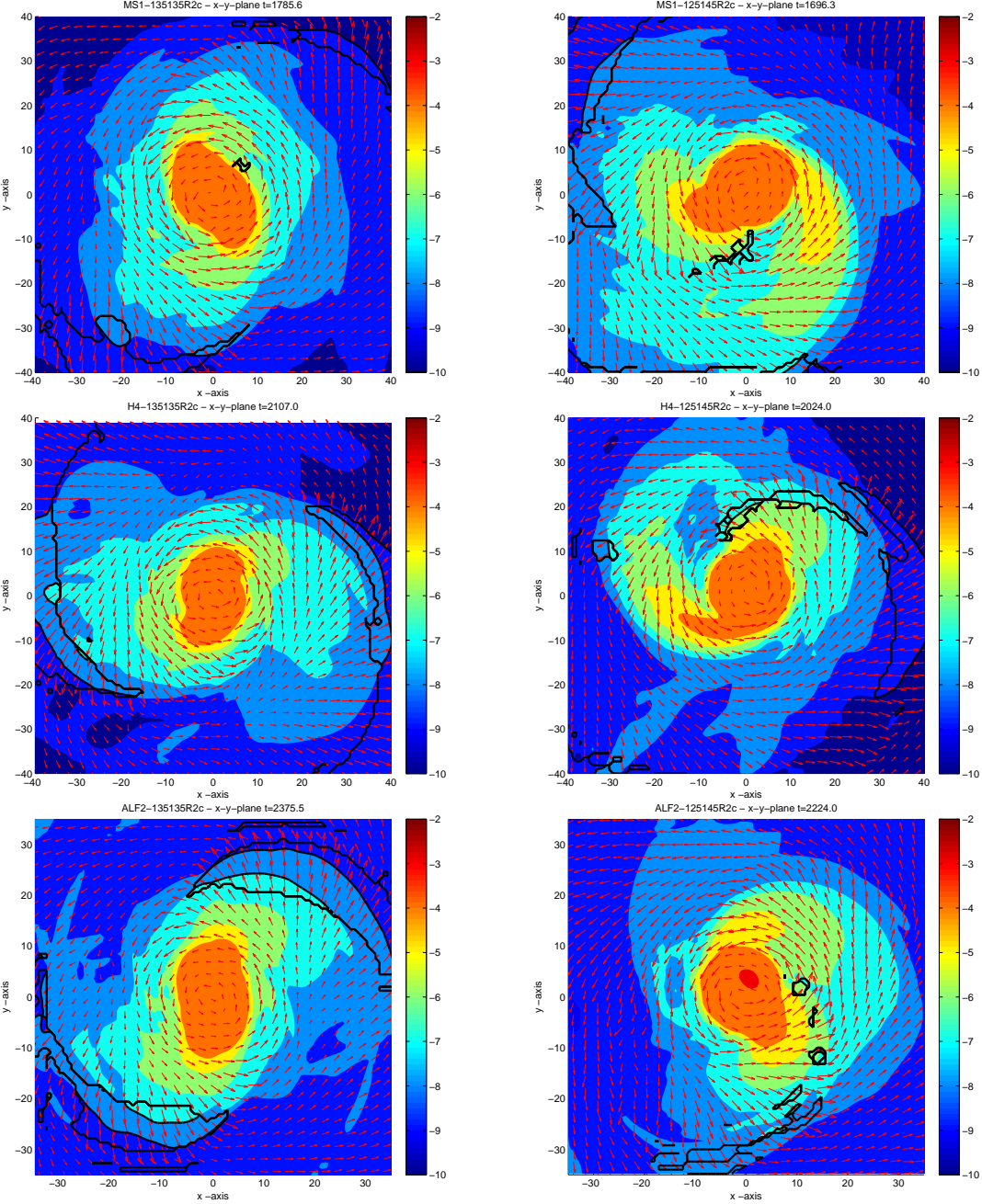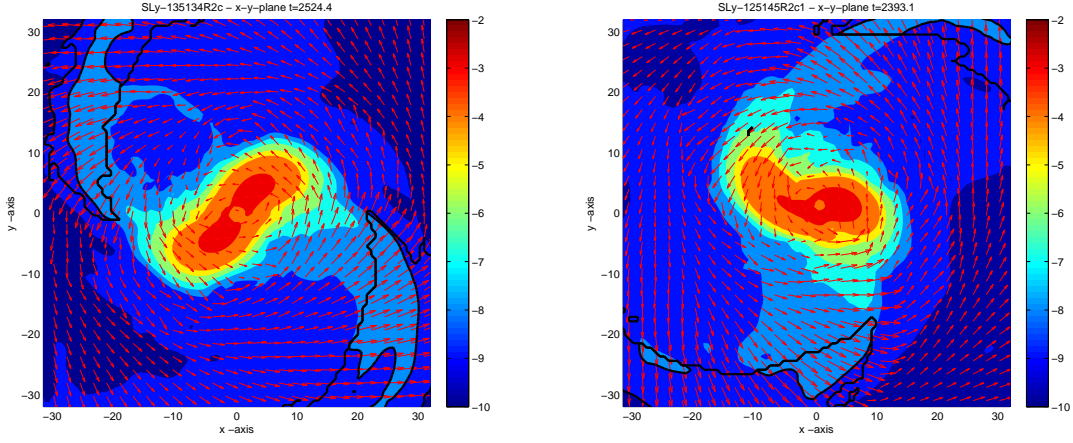
FIG. 9: 2D snapshot of density and velocity on the orbital plane shortly after the moment of merger. The velocity pattern is indicated by red arrows. The region inside the black contours contain unbound material on a logarithmic scale with $\rho_{ejecta} = (10^{-10}, 10^{-9}, 10^{-8}, 10^{-7}, 10^{-6}, 10^{-5})$. The logarithm of the density $\log_{10}(\rho)$ is visualized according to the color bar. Left (from top to bottom): MS1-135135-R2c, H4-135135-R2c, ALF2-135135-R2c, SLy-135135-R2c. Right (from top to bottom): MS1-125145-R2c, H4-125145-R2c, ALF2-125145-R2c, SLy-125145-R2c1.
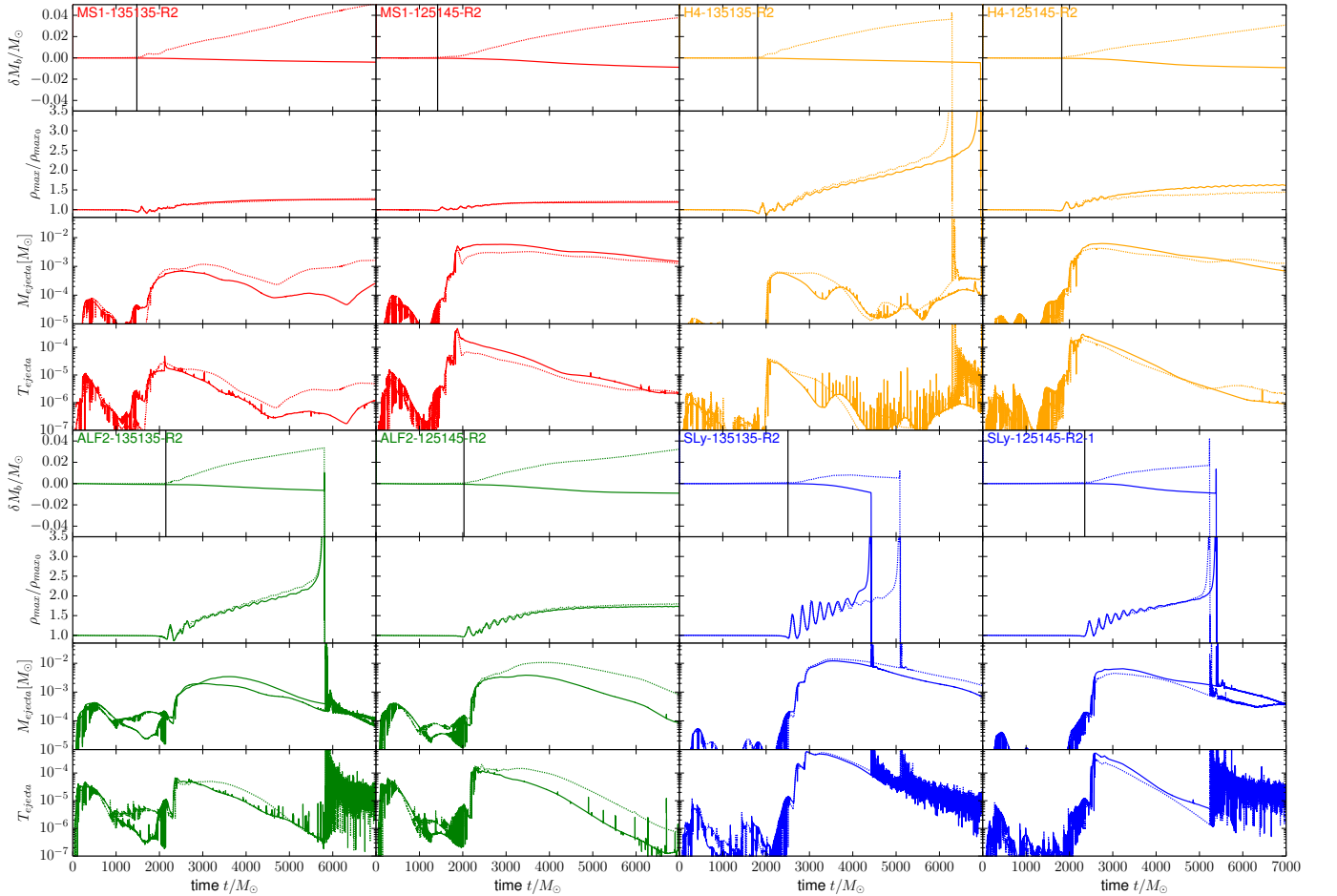
FIG. 10: Evolution of several dynamical quantities for $M = 2.7 M_\odot$ $q = 1, 1.16$ configurations. Results for different EOS are in different color. For each configuration, the panel contains four plots. From top to bottom: rest-mass violation $\delta M = M_b(t) - M_b(t=0)$ on level $l = 1$; maximum density $\rho_{max} = \max(\rho)$ on the grid scaled to its initial value $\rho_{max}(t)/\rho_{max}(t=0)$; rest-mass of the ejected material M_{ejecta}; kinetic energy of the ejecta T_{ejecta}. Results for the conservative AMR are presented with solid lines, while the corresponding results for the nonconservative AMR are shown with dashed lines. Vertical lines represent the moment of merger, i.e. t_{mrg} determined by the maximum in $|rh_{22}|$.
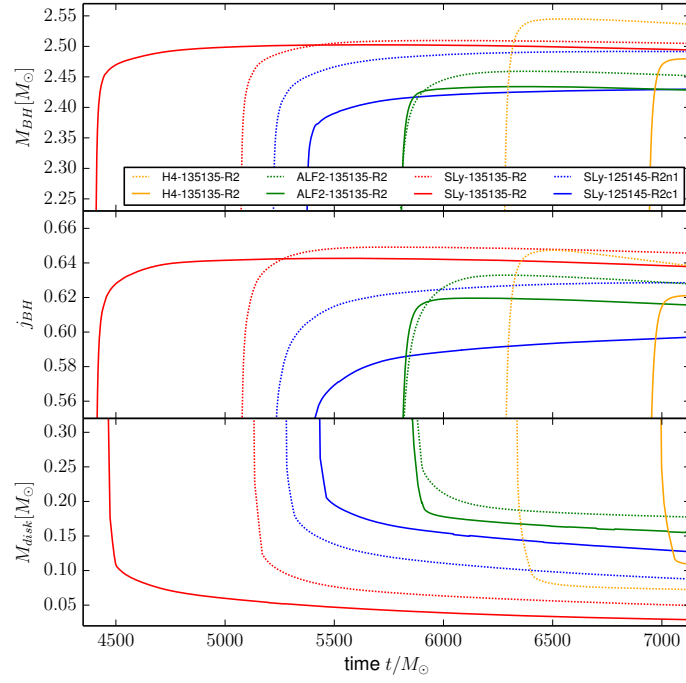
FIG. 11: Black hole and disk evolution for simulations with and without conservative AMR. Top: black hole horizon mass. Middle: black hole dimensionless angular momentum. Bottom: disk rest-mass.
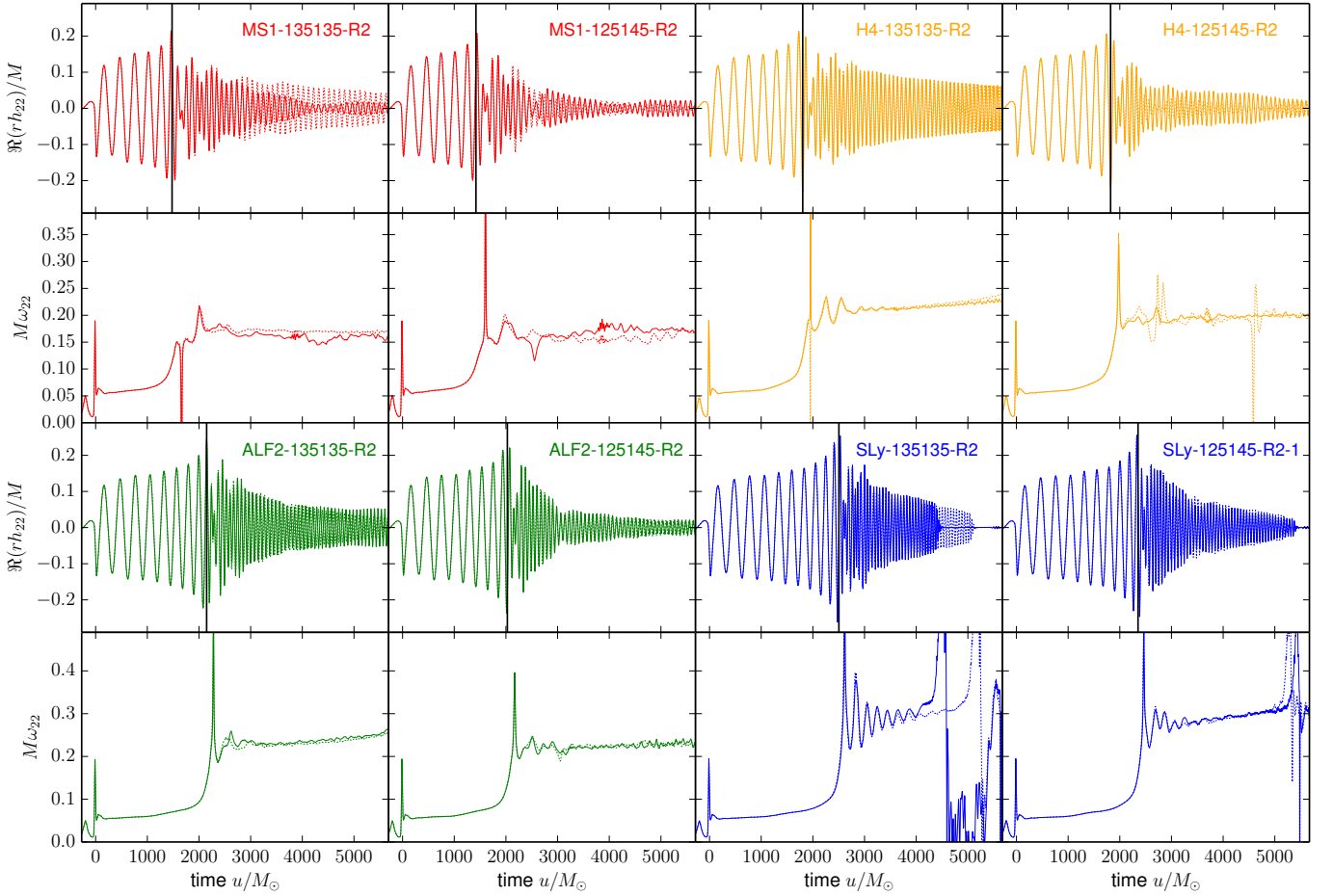
FIG. 12: Gravitational waves signals for $M = 2.7$ $q = 1, 1.16$ configurations. For each configuration, the panel contains two plots. Top: $\Re(rh_{22})$; Bottom: $M\omega_{22}$. Results for the conservative AMR are presented in solid lines, while the corresponding results for the nonconservative AMR are in dashed lines. Vertical lines mark the moment of merger, i.e. t_{mrg} determined by the maximum in $|rh_{22}|$.
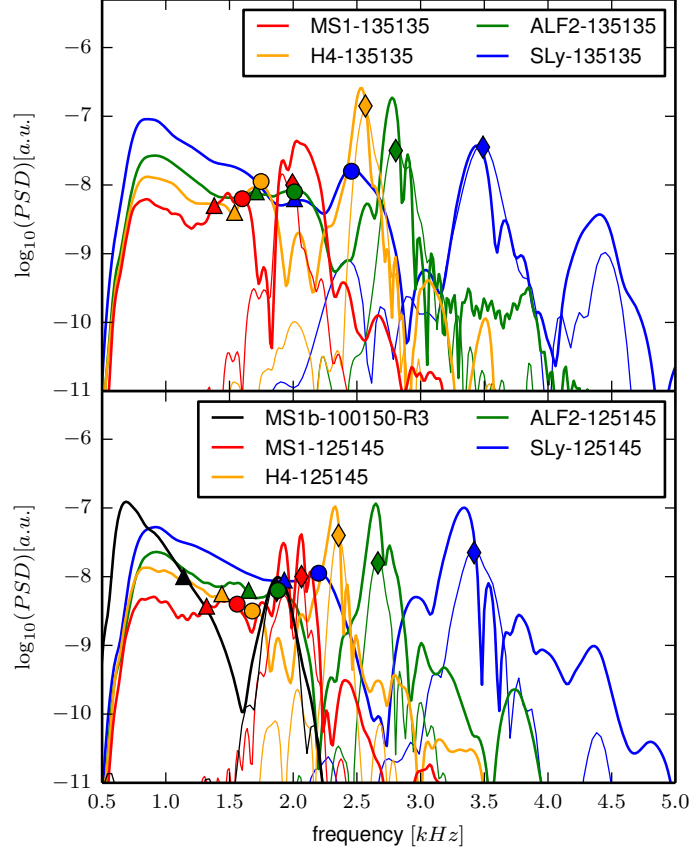
FIG. 13: Gravitational waves spectra for $M = 2.7$ $q = 1$ (top) and $q = 1.16$ (bottom) configurations. The colors correspond to Fig. 12: MS1b (red), ALF2 (orange), H4 (green), SLy (blue). The thick lines refer to the entire GW-signal, while the thin lines include only the GWs emitted after the moment merger $t > t_{\mathrm{mrg}}$. Important frequencies are marked in the plot: f_{mrg} (triangles), f_s (circles), and f_2 (diamonds). Additionally the MS1b-100150-R3c is added in the bottom panel. For this setup no clear f_s-frequency is visible.
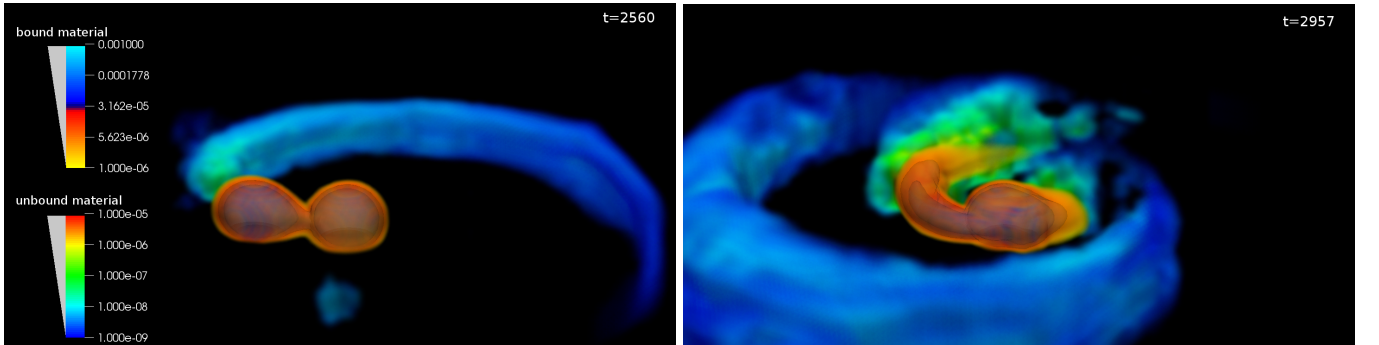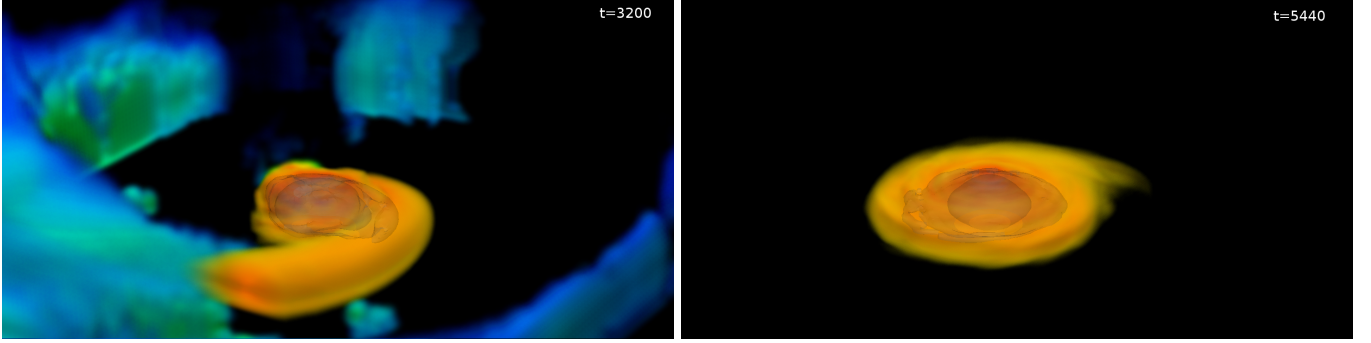
FIG. 14: The strong-field merger dynamics of MS1b-100150. The figure shows four snapshots of the bound and unbound density ρ at $t \sim 2560$ (top-left), $t \sim 2957$ (top-right), $t \sim 3200$ (bottom-left), and $t \sim 5440$ (bottom-right). All subplots contain the same contour range and the same part of the computational domain. The bound density ρ is shown on a logarithmic scale from 10^{-6} (yellow) to 10^{-3} (blue), and highlighted with contours for $\rho = (10^{-5}, 10^{-4}, 10^{-3})$. The unbound material is shown on a logarithmic scale from 10^{-9} (blue) to 10^{-5} (red). Top-left: About 1.5 orbit before the moment of merger the stars come in contact. At $t \sim 2560$ the companion ($M_B = 1 \, M_\odot$, left) is deformed by the tidal field of the primary ($M_A = 1.5 \, M_\odot$, right). Ejecta originate from the tidal tail of the companion, and are emitted around the orbital plane. Top-right: At $t \sim 2957$, shortly after the moment of merger, the companion is already partially disrupted, most of the ejecta is emitted around this time. Bottom-left: At $t \sim 3200$ material is also ejected by the shock-heating–driven mechanism described in the text in a direction perpendicular to the orbital plane. On larger scales (not shown in the plot) ejecta appear anisotropically distributed around the orbital plane with an opening angle $\sim 10°$. Bottom, right: The merger remnant is composed of a MNS with a high density core surrounded by an accretion disk of rest-mass $\sim 0.3 M_\odot$. The entire disk has a radius of $\sim 35 M_\odot \approx 55\text{km}$.
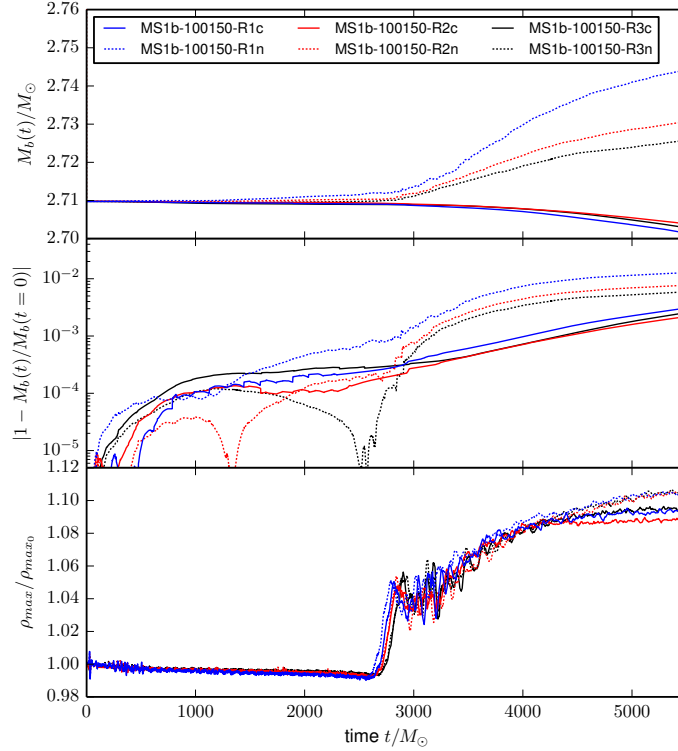
FIG. 15: Rest-mass conservation for MS1b-100150 and resolution study. The plot shows results using resolutions R1 (blue), R2 (red), R3 (black), and runs with and without the C step. Top: rest-mass; Middle: error of the rest-mass conservation; Bottom: maximum density $\rho_{max}(t)$ normalized by the initial maximum density $\rho_{max}(t = 0)$

x−y−plane t=2048.6

x−y−plane t=2793.6

x−z−plane t=2048.6

x−z−plane t=2793.6

x−y−plane t=2961.2

x−y−plane t=3031.1
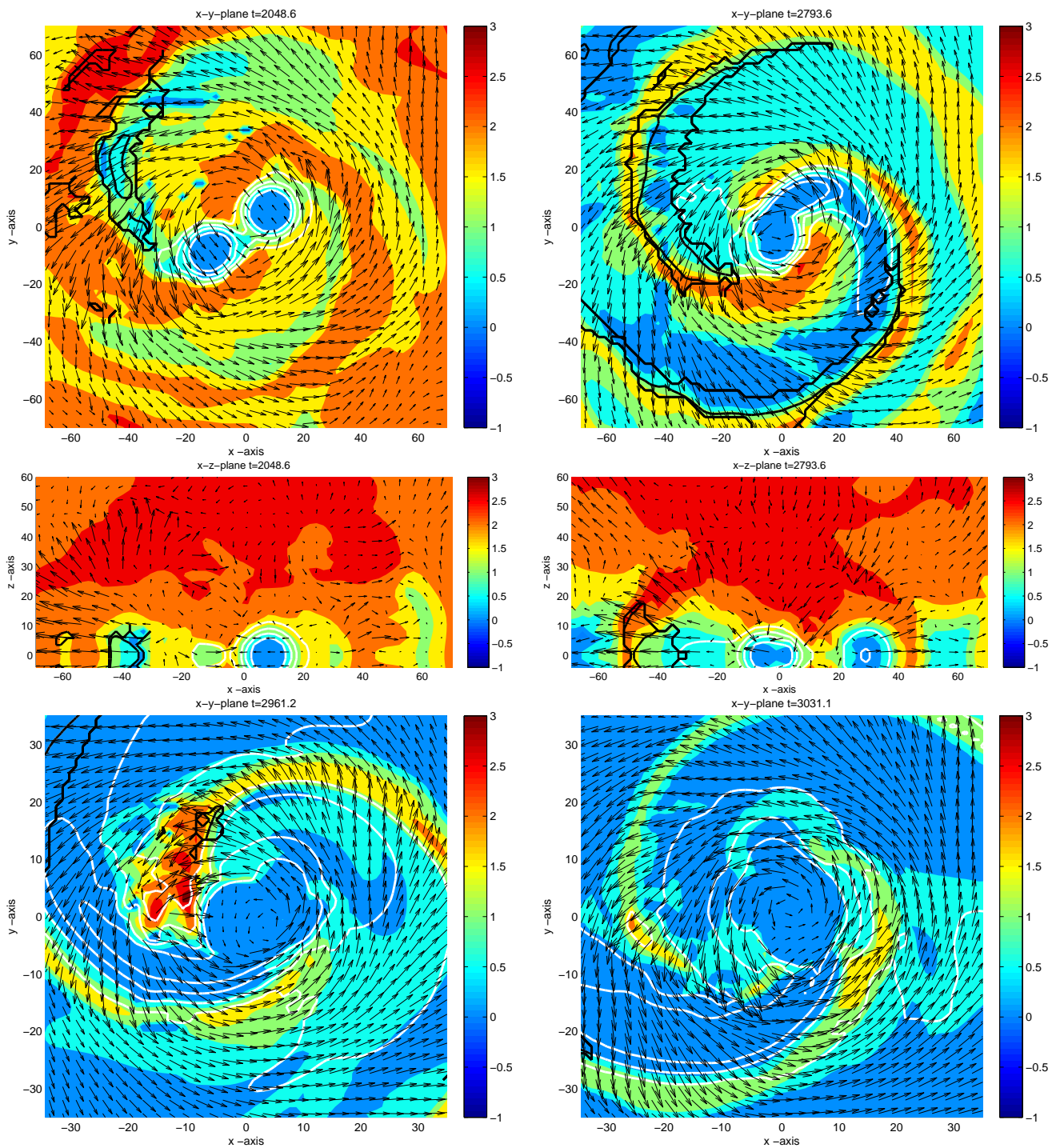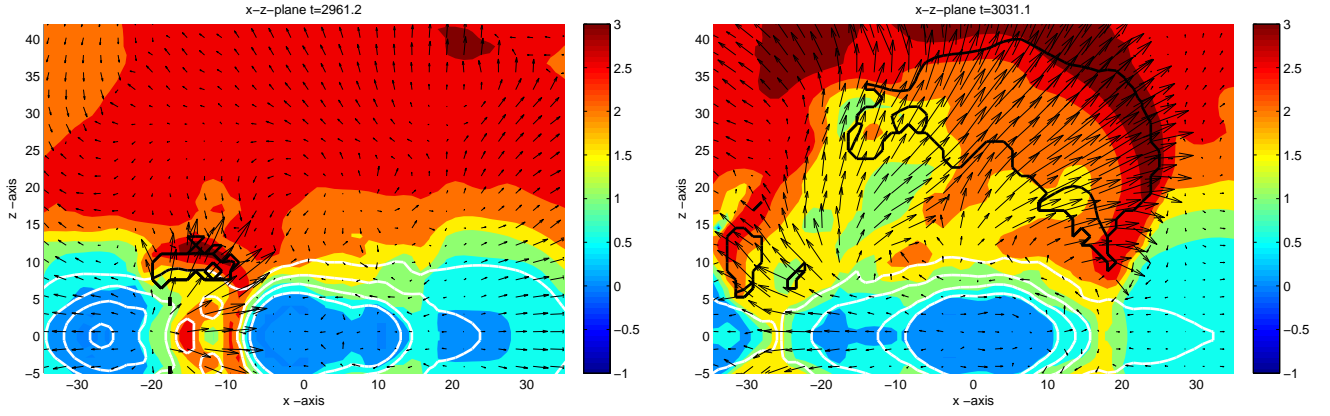
FIG. 16: Snapshots of the MS1b-100150-R1c evolution on the $(x, y, z = 0)$ and $(x, y = 0, x)$ planes for $t = 2016 M_\odot, 2794 M_\odot$ (upper panels) and $t = 2961 M_\odot, 3031 M_\odot$ (bottom panels). The density ρ is plotted in logarithmic scale with white contours shown at $\rho = (10^{-7}, 10^{-6}, 10^{-5}, 10^{-4}, 10^{-3})$, the ejecta are colored red (or black for better readability) at $\rho = (10^{-10}, 10^{-9}, 10^{-8}, 10^{-7}, 10^{-6})$, the velocity v^i is visualized by black arrows. The logarithm of the entropy indicator $\log_{10} \hat{S}$ is presented according to the color bar.
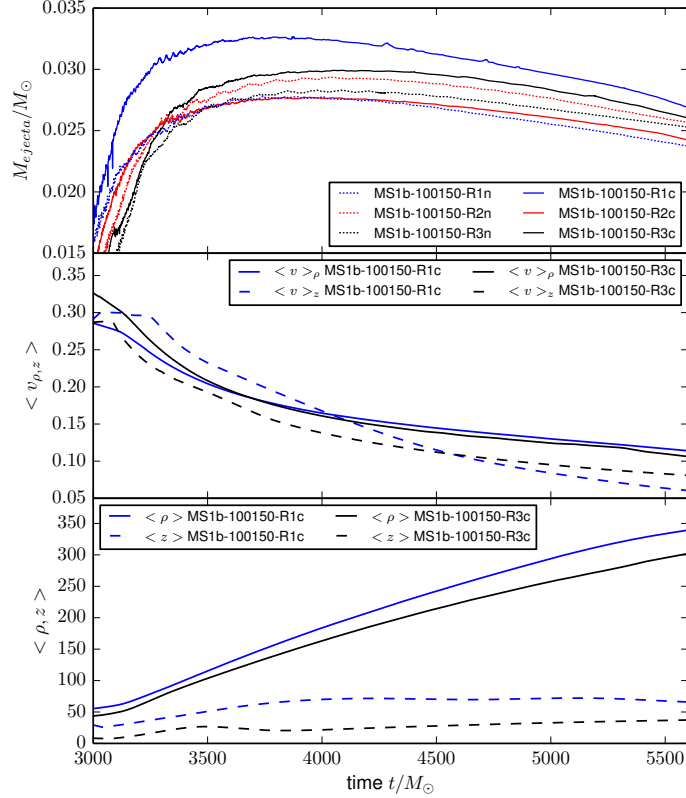
FIG. 17: Mass, average velocities and geometry of the ejected mass MS1b-100150. Top: Ejecta mass for all resolutions. Middle: $\langle v \rangle_{\rho, z}$ on the (x, y) plane and the (x, z) plane. Bottom: $\langle \rho \rangle, \langle z \rangle$. The middle and bottom panel are restricted to highest and lowest resolution only for better readability.
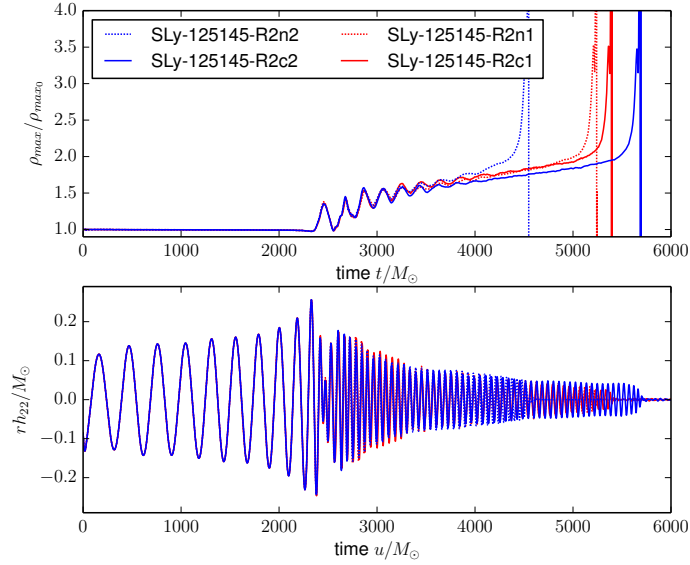
FIG. 18: SLy-125145-R2 configuration for different grid setups. Without the C step, a change in resolution and box size of 3% has a large influence on the lifetime of the HMNS.

Tables

TABLE I: Piecewise polytropic EOS parameters. For all EOSs we use a crust with $K_0 = 8.94746 \cdot 10^{-2}$ and $\Gamma_0 = 1.35692$, and $\rho_1 = 8.11940 \cdot 10^{-4}$; $\rho_2 = 1.62003 \cdot 10^{-3}$. Columns: EOS, the density were the crust ends, the polytropic exponents for the individual pieces Γ_i, the maximum supported gravitational mass M_{max}, the maximum supported baryonic mass, and the maximum adiabatic speed of sound $c_{s\ max}$ within the maximum stable neutron star configuration.

EOS	$\rho_0 \cdot 10^{-4}$	Γ_1	Γ_2	Γ_3	M_{max}	$M_{b\ max}$	$c_{s\ max}$
MS1b	1.84128	3.456	3.011	1.425	2.76	3.35	0.99
MS1	1.52560	3.224	3.033	1.325	2.77	3.35	1.00
H4	1.43830	2.909	2.246	2.144	2.03	2.33	0.72
ALF2	3.15535	4.070	2.411	1.890	1.99	2.32	0.65
SLy	2.36900	3.005	2.988	2.851	2.06	2.46	1.00

TABLE II: Summary of the combinations for restriction (R), prolongation (P), and mass correction (C) used in this work. AVG indicates average, LAG Lagrangian interpolation, WENO, WENOZ the interpolation method of [81, 84]. The order of convergence is reported for each RP operation.

Name	R	order	P	order	C
a2e2	AVG	2	ENO	2	✓
a2e2n	AVG	2	ENO	2	✗
a2wz6	AVG	2	WENOZ	6	✓
a2wz6n	AVG	2	WENOZ	6	✗
l4l4	LAG	4	LAG	4	✓
l4l4n	LAG	4	LAG	4	✗
w4w4	WENO	4	WENO	4	✓
w4w4n	WENO	4	WENO	4	✗

TABLE III: Grid and parameters configurations for single star tests. L denotes the total number of boxes, l^{mv} is the finest non-moving level. n (n^{mv}) is the number of points in the fixed (moving) boxes, h_0, h_{L-1} are the grid spacing in level $l = 0, L-1$ and , f_{atm} the atmosphere level, and f_{thr} the atmosphere threshold factor. The resolution in level l is $h_l = h_0/2^l$.

Single star test	L	l^{mv}	n	n^{mv}	h_0	h_{L-1}	f_{atm}	f_{thr}
TOV_{static}	5	-	56	56	2.0	0.125	10^{-9}	10^2
TOV_{static}	5	-	56	56	2.0	0.125	10^{-11}	10^2
TOV_{boost}	5	-	128	128	2.0	0.125	10^{-9}	10^2
TOV_{boost}	5	-	128	128	2.0	0.125	10^{-11}	10^2
TOV_{mig}	7	-	128	128	9.6	0.150	10^{-10}	10^2
TOV_{mig}	7	-	128	128	9.6	0.150	10^{-11}	10^2
TOV_{mig}	7	-	128	128	9.6	0.150	10^{-12}	10^2
TOV_{mig}	7	-	128	128	9.6	0.150	10^{-13}	10^2
TOV_{mig}	7	-	128	128	9.6	0.150	10^{-10}	10^1
TOV_{mig}	7	-	128	128	9.6	0.150	10^{-11}	10^1
TOV_{mig}	7	-	128	128	9.6	0.150	10^{-11}	10^3
TOV_{mig}	7	-	128	128	9.6	0.150	10^{-11}	10^4
$\mathrm{RNS}_{\mathrm{BU7}}$	6	1	128	64	2.0	0.0625	10^{-9}	10^2
$\mathrm{BU}_{\mathrm{Kep}}$	7	2	144	96	4.0	0.0625	10^{-9}	10^2

TABLE IV: Initial BNS configurations and grid setup. First column defines the configuration name. Next 11 columns describe the physical properties: EOS, gravitational mass of the individual stars $M_{A,B}$, baryonic mass of the individual stars $M_{b\ A,B}$, stars' compactnesses $\mathcal{C}_{A,B}$, tidal coupling constant κ_2^T, initial gravitational wave circular frequency $M\omega_{22}^0$, ADM-Mass M_{ADM}, ADM-angular momentum J_{ADM}. Next 8 columns describe the grid configuration: finest grid spacing h_{L-1}, radial resolution inside the shells h_r, number of points in the fix (moving) n (n^{mv}) levels, radial point number n_r and angular point number n_θ in the shells, inradius up to which GRHD equations are solved r_1, and boundary r_b. Notice that we divide the configurations in 3 different grid setups R1, R2, R3 (compare simulation name). All configurations are evolved with and without the C step, which we denote with a "c" or "n" in the configuration name.

Name	EOS	M_A	M_B	$M_{b\ A}$	$M_{b\ B}$	$\mathcal{C}_A$	$\mathcal{C}_B$	κ_2^T	$M\omega_{22}^0$	M_{ADM}	J_{ADM}	h_{L-1}	h_r	n	n^{mv}	n_r	n_θ	r_1	r_b
MS1-135135-R2c	MS1	1.35	1.35	1.46	1.46	0.139	0.139	325	0.052	2.676	7.16	0.240	7.68	160	80	160	70	614	1870
MS1-135135-R2n	MS1	1.35	1.35	1.46	1.46	0.139	0.139	325	0.052	2.676	7.16	0.240	7.68	160	80	160	70	614	1870
MS1-125145-R2c	MS1	1.45	1.25	1.61	1.38	0.148	0.129	331	0.052	2.673	7.10	0.240	7.38	160	80	160	70	590	1870
MS1-125145-R2n	MS1	1.45	1.25	1.61	1.38	0.148	0.129	331	0.052	2.673	7.10	0.240	7.38	160	80	160	70	590	1870
H4-135135-R2c	H4	1.35	1.35	1.47	1.47	0.147	0.147	210	0.052	2.674	7.13	0.2232	7.1424	160	80	160	70	571	1739
H4-135135-R2n	H4	1.35	1.35	1.47	1.47	0.147	0.147	210	0.052	2.674	7.13	0.2232	7.1424	160	80	160	70	571	1739
H4-125145-R2c	H4	1.45	1.25	1.59	1.35	0.158	0.136	212	0.052	2.674	7.10	0.230	7.36	160	80	160	70	589	1792
H4-125145-R2n	H4	1.45	1.25	1.59	1.35	0.158	0.136	212	0.052	2.674	7.10	0.230	7.36	160	80	160	70	589	1792
ALF2-135135-R2c	ALF2	1.35	1.35	1.49	1.49	0.161	0.161	138	0.052	2.675	7.15	0.202	6.464	160	80	160	70	517	1574
ALF2-135135-R2n	ALF2	1.35	1.35	1.49	1.49	0.161	0.161	138	0.052	2.675	7.15	0.202	6.464	160	80	160	70	517	1574
ALF2-125145-R2c	ALF2	1.45	1.25	1.61	1.37	0.172	0.150	140	0.052	2.673	7.08	0.200	6.4	160	80	160	70	512	1558
ALF2-125145-R2n	ALF2	1.45	1.25	1.64	1.37	0.172	0.150	140	0.052	2.673	7.08	0.200	6.4	160	80	160	70	512	1558
SLy-135135-R2c	SLy	1.35	1.35	1.49	1.49	0.174	0.174	74	0.052	2.675	7.15	0.1824	5.8368	160	80	160	70	467	1421
SLy-135135-R2n	SLy	1.35	1.35	1.49	1.49	0.174	0.174	74	0.052	2.675	7.15	0.1824	5.8368	160	80	160	70	467	1421
SLy-125145-R2c1	SLy	1.45	1.25	1.62	1.38	0.187	0.161	75	0.052	2.673	7.07	0.1824	5.8368	160	80	160	70	467	1421
SLy-125145-R2n1	SLy	1.45	1.25	1.62	1.37	0.187	0.161	75	0.052	2.673	7.07	0.1824	5.8368	160	80	160	70	467	1421
SLy-125145-R2c2	SLy	1.45	1.25	1.62	1.37	0.187	0.161	75	0.052	2.673	7.07	0.188	6.106	160	80	160	70	488	1464
SLy-125145-R2n2	SLy	1.45	1.25	1.62	1.37	0.187	0.161	75	0.052	2.673	7.07	0.188	6.106	160	80	160	70	488	1464
MS1b-100150-R1c	MS1b	1.50	1.00	1.64	1.06	0.157	0.109	461	0.042	2.479	6.16	0.291	9.312	128	64	128	56	596	1820
MS1b-100150-R1n	MS1b	1.50	1.00	1.64	1.06	0.157	0.109	461	0.042	2.479	6.16	0.291	9.312	128	64	128	56	596	1820
MS1b-100150-R2c	MS1b	1.50	1.00	1.64	1.06	0.157	0.109	461	0.042	2.479	6.16	0.2328	7.4496	160	80	160	70	596	1814
MS1b-100150-R2n	MS1b	1.50	1.00	1.64	1.06	0.157	0.109	461	0.042	2.479	6.16	0.2328	7.4496	160	80	160	70	596	1814
MS1b-100150-R3c	MS1b	1.50	1.00	1.64	1.06	0.157	0.109	461	0.042	2.479	6.16	0.194	6.208	192	96	192	84	596	1810
MS1b-100150-R3n	MS1b	1.50	1.00	1.64	1.06	0.157	0.109	461	0.042	2.479	6.16	0.194	6.208	192	96	192	84	596	1810

TABLE V: Summary of the numerical results for the $M = 2.7 M_\odot$-simulations. Columns: Simulation name, merger time, merger frequency (stated dimensionless and in Hz), final remnant, the lifetime of the HMNS τ_{HMNS} stated in solar masses and milliseconds, 2nd peak f_s- and f_2-mode frequency (dimensionless and in Hz), mass and kinetic energy of the ejected material M_{ejecta} (see Fig. 10), the mass of the disk surrounding the central object M_{disk} measured $\sim 200 M_\odot$ after BH formation, the black hole mass M_{BH} and its dimensionless angular momentum j_{BH}.

Name	t_{mrg}	$M\omega_{22}^{\mathrm{mrg}}$	f_{mrg} [kHz]	Remnant	τ_{HMNS} (ms)	$M\omega_{22}^s$	f_s [kHz]	$M\omega_{22}^2$	f_2 [kHz]	M_{ejecta} $[10^{-3}]$	T_{ejecta} $[10^{-4}]$ $(10^{50}$ erg)	M_{disk} $[10^{-2}]$	M_{BH}	j_{BH}
MS1-135135-R2c	1479	0.112	1.38	MNS	-	0.134	1.60	0.166	1.99	0.7	0.1 (0.2)	-	-	
MS1-135135-R2n	1476	0.114	1.36	MNS	-	0.135	1.61	0.170	2.04	1.2	0.1 (0.2)	-	-	
MS1-125145-R2c	1420	0.110	1.32	MNS	-	0.130	1.56	0.172	2.06	5.8	0.7 (1.2)	-	-	
MS1-125145-R2n	1419	0.111	1.33	MNS	-	0.125	1.50	0.157	1.88	3.2	0.2 (0.4)	-	-	
H4-135135-R2c	1804	0.129	1.54	HMNS→BH 5130 (25)		0.146	1.75	0.214	2.57	0.6	0.3 (0.5)	10.8	2.48	0.62
H4-135135-R2n	1803	0.130	1.55	HMNS→BH 4470 (22)		0.145	1.73	0.216	2.58	0.6	0.3 (0.6)	8.5	2.54	0.65
H4-125145-R2c	1822	0.120	1.44	HMNS	-	0.140	1.68	0.197	2.36	6.0	1.6 (2.8)	-	-	-
H4-125145-R2n	1820	0.120	1.44	HMNS	-	0.146	1.75	0.194	2.32	4.0	1.2 (2.3)	-	-	-
ALF2-135135-R2c	2148	0.142	1.71	HMNS→BH 3760 (19)		0.168	2.01	0.235	2.81	3.5	0.4 (0.7)	17.8	2.43	0.62
ALF2-135135-R2n	2145	0.142	1.71	HMNS→BH 3770 (19)		0.165	1.98	0.230	2.75	2.0	0.4 (0.7)	21.1	2.44	0.63
ALF2-125145-R2c	2028	0.138	1.65	HMNS	-	0.157	1.88	0.222	2.66	3.9	0.4 (0.8)	-	-	-
ALF2-125145-R2n	2027	0.139	1.66	HMNS	-	0.160	1.91	0.225	2.69	10.6	1.0 (1.9)	-	-	-
SLy-135135-R2c	2504	0.168	2.01	HMNS→BH 2159 (11)		0.206	2.46	0.292	3.49	12.2	4.0 (7.1)	8.4	2.48	0.64
SLy-135135-R2n	2495	0.168	2.01	HMNS→BH 2577 (13)		0.207	2.48	0.290	3.47	14.2	5.9 (10.5)	9.6	2.49	0.64
SLy-125145-R2c1	2353	0.162	1.93	HMNS→BH 3020 (15)		0.184	2.20	0.286	3.42	6.5	2.8 (5.1)	17.9	2.40	0.58
SLy-125145-R2n1	2350	0.161	1.93	HMNS→BH 2870 (14)		0.187	2.24	0.283	3.39	4.5	1.7 (3.0)	14.5	2.46	0.61
SLy-125145-R2c2	2350	0.161	1.92	HMNS→BH 3310 (16)		0.186	2.23	0.285	3.41	6.2	2.1 (3.7)	18.4	2.40	0.58
SLy-125145-R2n2	2348	0.160	1.91	HMNS→BH 2180 (11)		0.184	2.20	0.283	3.39	5.4	2.5 (4.5)	11.1	2.49	0.62

TABLE VI: Summary of the numerical results for the MS1b-100150 simulation. Columns: Grid identifier, time at merger t_{mrg}, GW frequency at merger stated dimensionless and in kHz, the peak frequency of the GW spectrum during the HMNS phase f_2 stated dimensionless and in kHz, and maximum mass of the ejected material M_{ejecta}.

Resolution	t_{mrg} $[M_\odot]$	$M\omega_{22}^{\mathrm{mrg}}$	f_{mrg} [kHz]	$M\omega_{22}^2$	f_2 [kHz]	M_{ejecta} $[10^{-3} M_\odot]$
R1c	2675	0.086	1.11	0.137	1.77	32.6
R1n	2640	0.085	1.10	0.139	1.79	27.8
R2c	2710	0.086	1.11	0.141	1.82	27.7
R2n	2701	0.085	1.10	0.140	1.81	29.4
R3c	2754	0.088	1.13	0.145	1.87	29.9
R3n	2757	0.088	1.14	0.142	1.83	28.3